

Hybrid upconverting/paramagnetic Fe₃O₄/Gd₂O₃:Er³⁺, Yb³⁺, Mg²⁺, Nd³⁺ nanoparticles – synthesis, characterization and biological applications

Izabela Kamińska^{1*} , Kamil Sobczak², Yaroslav Zhydashchyyk¹ , Tomasz Wojciechowski^{1,3} , Roman Minikayev¹ , Bożena Sikora-Dobrowolska¹ , Sabina Lewińska¹ , Michał Chojnacki^{1,3} , Krzysztof Fronc^{1,3}

¹Institute of Physics, Polish Academy of Sciences, al. Lotników 32/46, Warsaw 02-668, Poland

²Faculty of Chemistry, Biological and Chemical Research Centre, University of Warsaw, ul. Żwirki i Wigury 101, Warsaw 02-089, Poland

³International Research Centre MagTop, al. Lotników 32/46, Warsaw 02-668, Poland

Article info

Article history:

Received 04 Sep. 2023

Received in revised form 27 Feb. 2024

Accepted 07 Mar. 2024

Available on-line 12 Apr. 2024

Keywords:

Core/shell nanoparticles;
upconversion;
co-precipitation methods;
HeLa tumor cells;
confocal microscopy;
paramagnetic.

Abstract

The goals of this work are to design and develop a technology for fabrication and study of multifunctional properties of core/shell nanoparticles (NPs) as magnetic/luminescent markers. The new hybrid core/shell Fe₃O₄/Gd₂O₃:1% Er³⁺, 18% Yb³⁺, 2.5% Mg²⁺, x% Nd³⁺ NPs doped with different concentrations of neodymium ions, where x = 0%, 0.5%, 0.75%, 1%, 2%, 4%, were synthesized by the co-precipitation method. The NPs were characterised using XRD, TEM, SEM, EDX, confocal microscopy and photoluminescence. Fe₃O₄ (core) consists of several 13 nm NPs. The core/shell NPs have sizes from 220 nm to 641 nm. In this latter case, the shell thicknesses were 72, 80, and 121 nm. The upconversion efficiency properties and magnetic properties of the hybrid NPs were investigated. In the core/shell NPs, the addition of Nd³⁺ quenches the luminescence. The magnetic response of core/shell samples is rather paramagnetic and does not differ significantly from that registered for the shell material alone. For Gd₂O₃:1% Er³⁺, 18% Yb³⁺ and Fe₃O₄/Gd₂O₃:1% Er³⁺, 18% Yb³⁺, 2.5% Mg²⁺, 0.5% Nd³⁺, at 300 K, the values of the magnetization registered at ~40 kOe are similar and equal to ~5.3 emu·g⁻¹. The survivability of the HeLa tumor cells with the presence of the core/shell NPs was investigated for 24 h. The NPs are non-toxic up to a concentration of 1000 μg·ml⁻¹ and penetrate cells in the process of endocytosis which has been confirmed by confocal microscope studies.

1. Introduction

The work aimed to develop a technology for obtaining core/shell oxide nanoparticles (NPs) exhibiting anti-Stokes emission and at the same time possessing magnetic properties. The reason for undertaking this research topic was the need to produce spherical, separate, and hybrid NPs in quantities of several grams. The Gd₂O₃:Yb, Er, Mg, Nd layer is responsible for the NP visible light (560 nm and 660 nm) emission (luminescence) when illuminated with near infrared (NIR – 980 nm). This process is called upconversion. Radiation at 980 nm and 660 nm is poorly

absorbed by the body tissues, so the NPs luminescence through the skin from a depth of up to 3 cm can be observed. The upconversion process is a process with low quantum efficiency (of the order of tenths of a percent) which due to the very narrow radiation absorption spectrum by Yb ions requires the use of lasers. Thanks to the use of laser radiation from the NIR region (980 nm, 808 nm), autofluorescence from biological objects cannot be observed. Excitation radiation is not scattered due to the long wavelength and despite the low quantum efficiency of the upconversion process, a high signal-to-noise ratio can be observed [1, 2].

The advantage of the obtained core/shell oxide NPs will be the possibility of using them, thanks to the presence of Fe

*Corresponding author at: ikaminska@ifpan.edu.pl

and Gd ions [3, 4] as improved contrast in magnetic resonance imaging (MRI), and after attaching antibodies to their surface, they will become a cancerous cell-destroying factor, thanks to hyperthermia.

In their research, the authors use NPs based on an oxide matrix because a) the authors' technology allows the synthesis of NPs with sizes of 200 nm and more; b) according to Ref. 5, NPs of these sizes are ideal for tumor delivery (the influence of size, shape, etc.); c) they can be produced in large quantities (a typical process produces gram quantities [~ 2 g]), which is not possible in the case of fluorides. Additionally, the obtained hybrid NPs mainly consist of gadolinium ions, which are used in MRI.

A new application is the use of opto-magnetic NPs coated with antibodies in flow cytometry combined with dialysis, in a strong magnetic field to remove circulating cancer cells from the bloodstream that are the source of metastases.

The work is also distinguished by the fact that the core is not one large NP, but consists of small NPs, which ensures that the system is paramagnetic.

Several different routes have been used to synthesize bifunctional magnetic luminescent nanocomposite. Peng *et al.* [6] synthesized down converting $\text{Fe}_3\text{O}_4/\text{Gd}_2\text{O}_3:\text{Eu}^{3+}$ nanocomposites obtained by the homogeneous precipitation method. Shabanzadeh-Kouyakhi *et al.* [7] worked on Gd_2O_3 NPs that were coated with a Fe_3O_4 nanolayer synthesized via coprecipitation, and the resulting core/shell nanocomposites were encapsulated in a dextrose capping agent for enhanced biocompatibility. Chame *et al.* [8] characterised multifunctional composites based on core/shell $\text{Ag}/\text{Fe}_3\text{O}_4/\text{Gd}_2\text{O}_3:\text{Er}^{3+}$ NPs. They exhibited bactericidal properties of $\text{Ag}/\text{Fe}_3\text{O}_4$ with the enhancement of fluorescence intensity produced by Er^{3+} doped in a Gd_2O_3 matrix. Shen *et al.* [9] report the superparamagnetic and upconversion emitting $\text{Fe}_3\text{O}_4/\text{NaYF}_4:\text{Yb}$, Er hetero-NPs synthesized by a novel ligand anchoring strategy. Tejeda *et al.* [10] described a highly luminescent $\text{Y}_3\text{Al}_5\text{O}_{12}:\text{Nd}^{3+}$ nanophosphors that were synthesized using a sol-gel route and were subsequently mixed with superparamagnetic Fe_3O_4 NPs producing a core-shell structure. Jing *et al.* [11] obtained bifunctional core-shell $\text{Fe}_3\text{O}_4/\text{SiO}_2/\text{Gd}_2\text{O}_3:\text{Yb}$, Er nanostructures. Vu *et al.* [12] fabricated bifunctional optical-magnetic $\text{Fe}_3\text{O}_4/\text{Gd}_2\text{O}_3:\text{Er}^{3+}$, Li^+ . The upconversion emission intensity was significantly enhanced compared to that without Li^+ ions. In the work of Wu *et al.* [13], bifunctional core/shell down converting nanocomposites of $\text{Fe}_3\text{O}_4/\text{Gd}_2\text{O}_3:\text{Eu}^{3+}$ were synthesized through the urea homogeneous precipitation method. The influence of the pH value of the solution on the luminescence of the nanocomposite was examined.

In the research, the authors chose the Gd_2O_3 matrix because it has low phonon energy (phonon cut-off ~ 600 cm^{-1}), large bandgap (~ 5.4 eV), and high refractive index (> 1.9) [14]. The low phonon energy reduces the chances of multiphonon relaxation processes and enhances the efficiency of the upconversion radiative emissions [15]. Gd_2O_3 NPs were doped with Er^{3+} and Yb^{3+} rare earth and alkaline earth metal ions – Mg^{2+} to improve the luminescence efficiency [16]. The $\text{Gd}_2\text{O}_3:1\% \text{Er}^{3+}$, $18\% \text{Yb}^{3+}$, $2.5\% \text{Mg}^{2+}$ NPs were additionally doped with neodymium ions ($x\% \text{Nd}^{3+} = 0, 0.5\%, 0.75\%, 1\%, 2\%, 4\%$).

Thanks to this, NPs can be excited with the semiconductor lasers with two wavelengths of 980 nm (cross-transfer between $\text{Er}^{3+} - \text{Yb}^{3+} - \text{Nd}^{3+}$ ions) and with a wavelength of 808 nm (Nd^{3+}). The process of anti-Stokes emission from the Yb^{3+} ion, which has only one excited state (${}^2\text{F}_{5/2}$) corresponding to the absorption of about 980 nm from ${}^2\text{F}_{7/2}$ to ${}^2\text{F}_{5/2}$, involves the risk of heating biological samples.

The advantage of doping samples with Nd^{3+} ions is the shifting of the excitation wavelength to approximately 808 nm, which significantly reduces the effect of overheating. The water absorption coefficient at 980 nm is 0.48 cm^{-1} , while the water absorption coefficient at 808 nm is much lower and amounts to 0.02 cm^{-1} [17, 18]. The Nd^{3+} ions also have a higher absorption cross-section at 808 nm, (which is $1.2 \cdot 10^{-19}$ cm^2 [19]) than Yb^{3+} ions at 980 nm ($1.2 \cdot 10^{-20}$ cm^2 [20]).

In this work, $\text{Gd}_2\text{O}_3:1\% \text{Er}^{3+}$, $18\% \text{Yb}^{3+}$, $2.5\% \text{Mg}^{2+}$, $x\% \text{Nd}^{3+}$ ($x = 0\%, 0.5\%, 0.75\%, 1\%, 2\%, 4\%$) NPs and hybrid core/shell $\text{Fe}_3\text{O}_4/\text{Gd}_2\text{O}_3:1\% \text{Er}^{3+}$, $18\% \text{Yb}^{3+}$, $2.5\% \text{Mg}^{2+}$, $x\% \text{Nd}^{3+}$ NPs were synthesized and characterised. The core of the authors' hybrid NPs consists of a conglomerate of several Fe_3O_4 NPs. In the work of Shen *et al.* [21], a significant increase can be seen in the NIR absorption at 808 nm for the conglomerate Fe_3O_4 NPs in comparison to individual Fe_3O_4 NPs. As a result, hybrid NPs are more effective in photothermal therapies.

The effect of doping with neodymium ions on the anti-Stokes emission of $\text{Gd}_2\text{O}_3:1\% \text{Er}^{3+}$, $18\% \text{Yb}^{3+}$ and $\text{Fe}_3\text{O}_4/\text{Gd}_2\text{O}_3:1\% \text{Er}^{3+}$, $18\% \text{Yb}^{3+}$, $2.5\% \text{Mg}^{2+}$ NPs was examined. The influence of the thickness of the $\text{Gd}_2\text{O}_3:1\% \text{Er}^{3+}$, $18\% \text{Yb}^{3+}$ shell on the optical properties of $\text{Fe}_3\text{O}_4/\text{Gd}_2\text{O}_3:1\% \text{Er}^{3+}$, $18\% \text{Yb}^{3+}$ NPs was also investigated. NPs were synthesized by homogeneous precipitation methods and characterised by transmission electron microscopy (TEM), energy dispersive X-ray spectroscopy (EDX), scanning electron microscopy (SEM), X-ray diffraction (XRD), and photoluminescence (PL).

2. Experiment

2.1. Synthesis of $\text{Gd}_2\text{O}_3:\text{Er}^{3+}$, Yb^{3+} ; $\text{Gd}_2\text{O}_3:\text{Er}^{3+}$, Yb^{3+} , Mg^{2+} ; $\text{Gd}_2\text{O}_3:\text{Er}^{3+}$, Yb^{3+} , Nd^{3+} and $\text{Gd}_2\text{O}_3:\text{Er}^{3+}$, Yb^{3+} , Mg^{2+} , Nd^{3+} NPs

In this study, the authors successfully synthesized $\text{Gd}_2\text{O}_3:1\% \text{Er}^{3+}$, $18\% \text{Yb}^{3+}$ NPs; $\text{Gd}_2\text{O}_3:1\% \text{Er}^{3+}$, $18\% \text{Yb}^{3+}$, $2.5\% \text{Mg}^{2+}$ NPs; $\text{Gd}_2\text{O}_3:1\% \text{Er}^{3+}$, $18\% \text{Yb}^{3+}$ NPs doped with various concentrations of Nd^{3+} (0.5%, 0.75%, 1%, 2%, 4%) and $\text{Gd}_2\text{O}_3:1\% \text{Er}^{3+}$, $18\% \text{Yb}^{3+}$, $2.5\% \text{Mg}^{2+}$ NPs doped with various concentrations of Nd^{3+} (0.5%, 0.75%, 1%, 2%, 4%) using homogeneous precipitation synthesis [Supporting Information (SI) Table S1].

Each synthesis was carried out in a shaking water bath for 2 h at a temperature of 90 °C. The hydrolysis of urea produces an amorphous powder, hydrated $\text{Gd}(\text{OH})\text{CO}_3$ doped with rare earth ions and/or alkali metals. After synthesis, the precipitates were washed five times with deionized water. Centrifugation parameters: 6000 rpm, 15 °C, 15 min. In order to crystallize and calcinate the material, NPs were heated in a furnace, in air, for 2 h at a temperature of 700 °C.

2.2. Synthesis of magnetic Fe₃O₄ NPs

A mixture of 2.36 g FeCl₃·6H₂O and 0.86 g FeCl₂·4H₂O was used for the synthesis of Fe₃O₄ NPs. The reagents were mixed in 40 ml of deionized water and stirred under an argon atmosphere. Then, 5 ml of ammonium hydroxide 28–30% was added and it was quickly stirred (350 rpm) at a temperature of 90 °C. 1.3 g of poly (ethylene glycol) PEG 4600 was dissolved in 5 ml of deionized water and the solution was added drop by drop to the remaining reaction components. The solution was stirred at 90 °C for 1 h. A black precipitate was obtained which was washed several times with deionized water. Centrifugation parameters: 6000 rpm, 15 °C, 15 min. Finally, the precipitate was washed with ethanol (99.8%) and dried in a laboratory furnace overnight. A total amount of 1 g of NPs was obtained.

2.3. Synthesis of Fe₃O₄/Gd₂O₃:Er³⁺, Yb³⁺ NPs

For the synthesis of Fe₃O₄/Gd₂O₃:1% Er³⁺, 18% Yb³⁺ NPs, 30 mg of Fe₃O₄ NPs was used, which was dissolved in 100 ml of deionized water and sonicated in an ultrasonic bath for 30 min. 10 ml of this solution was taken for further steps of the synthesis. Then, 0.76 g of gadolinium nitrate Gd(NO₃)₃·6H₂O, 4.49 mg of erbium nitrate Er(NO₃)₃·5H₂O, 0.08 g of ytterbium nitrate Yb(NO₃)₃·5H₂O, and 2.5 g of urea CO(NH₂)₂ as reducer were added to the conical flask. Everything was dissolved in 100 ml of distilled water. The synthesis was carried out for 1 h, 2 h, 3 h, 4 h at 90 °C in a water bath with shaking (120 rpm). The synthesis was carried out at different times to obtain different thicknesses of Gd₂O₃:Er³⁺, Yb³⁺ shells. A white-brown precipitate was obtained, which was then centrifuged and purified three times with deionized water in a laboratory centrifuge, centrifugation parameters: 6000 rpm, 15 °C, 15 min. The NPs were dried overnight in a laboratory dryer at 80 °C and calcined in a furnace, in air, at 700 °C for 2 h.

2.4. Synthesis of Fe₃O₄/Gd₂O₃:Er³⁺, Yb³⁺, Mg²⁺, Nd³⁺ NPs

For the synthesis of Fe₃O₄/Gd₂O₃:1% Er³⁺, 18% Yb³⁺, 2.5% Mg²⁺, x% Nd³⁺ NPs, 30 mg of Fe₃O₄ NPs were used, which was dissolved in 100 ml of deionized water and sonicated for 30 min in water in an ultrasonic bath. 100 ml of this solution was added to the synthesis. Then, oxidants were added to the Fe₃O₄ nanoparticle solution, i.e., 7.64 g of gadolinium nitrate Gd(NO₃)₃·6H₂O, 44.9 mg of erbium nitrate Er(NO₃)₃·5H₂O and various amounts (0.02 g, 0.03 g, 0.04 g, 0.08 g, 0.17 g) of neodymium nitrate Nd(NO₃)₃·6H₂O, 0.064 g of magnesium nitrate Mg(NO₃)₂·6H₂O, 0.8 g of ytterbium nitrate Yb(NO₃)₃·5H₂O. Finally, 25.4 g of urea CO(NH₂)₂ reducer was added. The synthesis was carried out in a shaking water bath for 2 h at a temperature of 90 °C. After synthesis, the precipitate was washed five times in deionized water. Centrifugation parameters: 6000 rpm, 15 °C, 15 min. The white-brown precipitate was dried in a laboratory furnace overnight. In order to crystallize the material, Fe₃O₄/Gd₂O₃:1% Er³⁺, 18% Yb³⁺, 2.5% Mg²⁺, x% Nd³⁺ NPs were calcined in a furnace, in air, for 2 h at 700 °C.

3. Results and discussion

3.1. Characterisation

The crystal structure and lattice parameters of NPs were analysed by X-ray diffraction. Details regarding XRD, SEM, and TEM measurements are described in SI. The produced Fe₃O₄ NPs have a cubic crystal structure (symmetry group Fd-3m) [Fig. 1(a)]. The lattice parameter *a* is 8.35271 Å ± 0.00047 Å, whereas the Gd₂O₃:1% Er³⁺, 18% Yb³⁺, 0.5% Nd³⁺ and Gd₂O₃:1% Er³⁺, 18% Yb³⁺, 2.5% Mg²⁺, 0.5% Nd³⁺ NPs have a cubic Gd₂O₃ crystal structure (symmetry group Ia-3) (SI Fig. S1). The lattice parameter *a* in this case is 10.7816 Å ± 0.0003 Å and 10.7799 Å ± 0.0003 Å, respectively. The obtained Fe₃O₄/Gd₂O₃:1% Er³⁺, 18% Yb³⁺, 2.5% Mg²⁺, 0.5% Nd³⁺ NPs have a cubic Gd₂O₃ crystal structure (symmetry group Ia-3) [Fig. 1(b)]. The lattice parameter *a* in this case is 10.7869 Å ± 0.0005 Å.

EDX maps of Fe₃O₄ NPs were performed as shown in SI Fig. S2(b)–(d). Analogous EDX maps of elements such as iron (Fe) and oxygen (O), and ytterbium (Yb) were made for the following NPs: Fe₃O₄/Gd₂O₃:1% Er³⁺, 18% Yb³⁺, 2.5% Mg²⁺, 0.5% Nd³⁺, Fe₃O₄/Gd₂O₃:1% Er³⁺, 18% Yb³⁺,

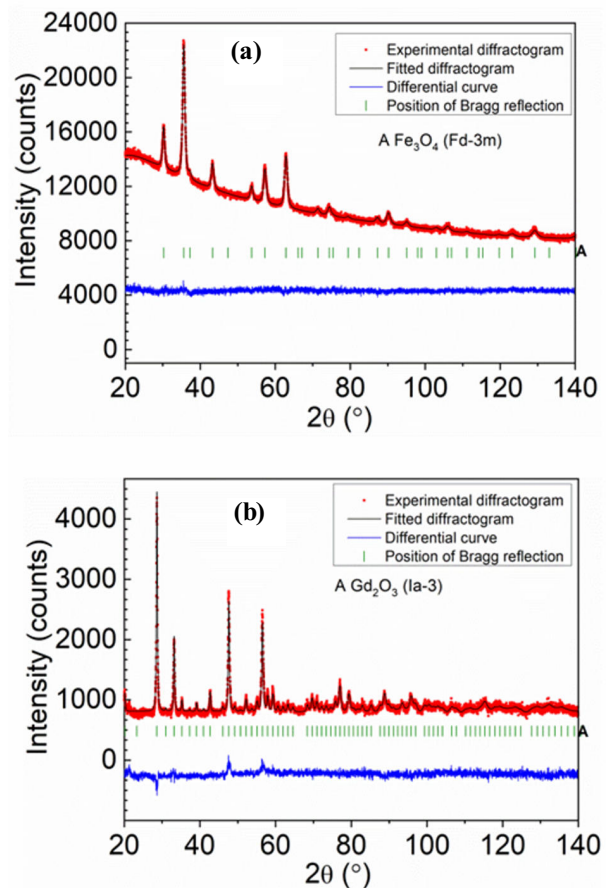


Fig. 1. Experimental X-ray diffractograms measured for (a) Fe₃O₄; (b) Fe₃O₄/Gd₂O₃:1% Er³⁺, 18% Yb³⁺, 2.5% Mg²⁺, 0.5% Nd³⁺ NPs and matched using the Rietveld method theoretical diffractograms. Symbols: (•) experimental and (—) fitted diffractograms, (—) differential curve and (|) positions of Bragg reflections (coming from Fe₃O₄ and Gd₂O₃ phases, respectively).

2.5% Mg²⁺, 0.75% Nd³⁺ and Fe₃O₄/Gd₂O₃:1% Er³⁺, 18% Yb³⁺, 2.5% Mg²⁺, 1% Nd³⁺ NPs as shown in Fig. 2, SI Fig. S3(a)–(h), SI Fig. S4(c)–(h), and SI Fig. S5(c)–(h), respectively.

The average sizes of Fe₃O₄; Fe₃O₄/Gd₂O₃:1% Er³⁺, 18% Yb³⁺, 2.5% Mg²⁺, 0.75% Nd³⁺; Fe₃O₄/Gd₂O₃:1% Er³⁺, 18% Yb³⁺, 2.5% Mg²⁺, 1% Nd³⁺, and Fe₃O₄/Gd₂O₃:1% Er³⁺, 18% Yb³⁺, 2.5% Mg²⁺, 1% Nd³⁺ NPs were determined using TEM. The NPs are of sizes of 13 nm, 223 nm, 244 nm, and 317 nm, respectively, as shown in SI Fig. S6(e), Fig. 2(b), SI Fig. S4(j), and SI Fig. S5(j).

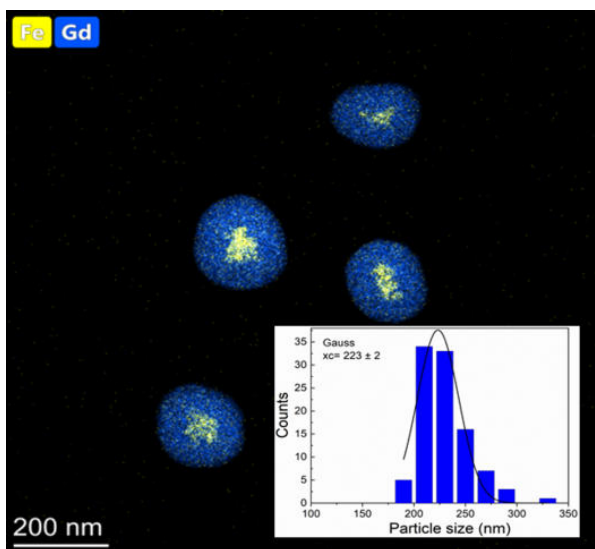


Fig. 2. Core/shell Fe₃O₄/Gd₂O₃:1% Er³⁺, 18% Yb³⁺, 2.5% Mg²⁺, 0.5% Nd³⁺ NPs Fe/Gd distribution analysis. The composite EDX map of Fe (yellow) and Gd (blue). Inset: histogram of the NPs size distribution.

The size of NPs and their morphology were also examined by SEM as shown in Fig. 3(a)–(g), SI: Fig. S7(a)–(h), Fig. S8(a)–(h), Fig. S9(a)–(b), Fig. S10(a)–(h), Table S2, Table S4, and Table S5. Histograms of the size distributions for the NPs are shown in SI: Fig. S11(a)–(h), Fig. S12(a)–(h), Fig. S13(a)–(b), Fig. S14(a)–(h), Fig. S15(a)–(d), and Fig. S16(a)–(c). The obtained NPs are separate and spherical.

3.2. Optical properties

3.2.1. Optical properties of Gd₂O₃:1% Er³⁺, 18% Yb³⁺, x% Nd³⁺ NPs

The Gd₂O₃:1% Er³⁺, 18% Yb³⁺, x% Nd³⁺ NPs exhibit luminescence in the visible region at a wavelength of 560 nm and 660 nm after excitation with a laser at a wavelength of 980 nm (continuous wave laser), which corresponds to the characteristic transitions in Er³⁺ ions, ⁴F_{9/2}→⁴I_{15/2}, and ⁴S_{3/2}→⁴I_{15/2}, ²H_{11/2}→⁴I_{15/2}, respectively.

The highest red luminescence was observed for NPs not doped with neodymium, for a laser power density of 4.52 W·cm⁻² [Fig. 4(a)]. Examples of luminescence spectra of Gd₂O₃:1% Er³⁺, 18% Yb³⁺, 0.5% Nd³⁺ NPs measured for five 980 nm laser power densities (4.52 W·cm⁻², 5.92 W·cm⁻², 11.98 W·cm⁻², 16.73 W·cm⁻²

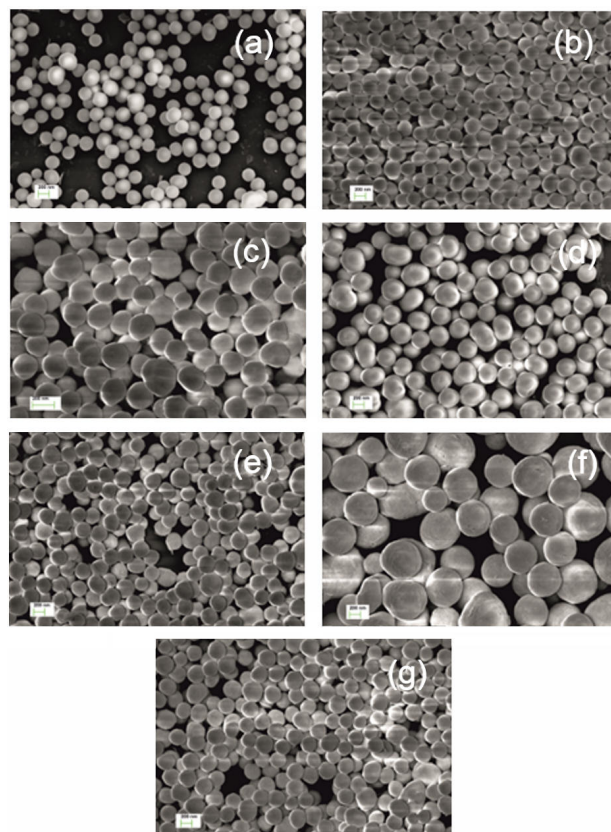


Fig. 3. SEM images of (a) Fe₃O₄/Gd(OH)CO₃:1% Er³⁺, 18% Yb³⁺, 2.5% Mg²⁺, 0.5% Nd³⁺, (b) Fe₃O₄/Gd(OH)CO₃:1% Er³⁺, 18% Yb³⁺, 2.5% Mg²⁺, 0.75% Nd³⁺, (c) Fe₃O₄/Gd₂O₃:1% Er³⁺, 18% Yb³⁺, 2.5% Mg²⁺, 0.75% Nd³⁺, (d) Fe₃O₄/Gd(OH)CO₃:1% Er³⁺, 18% Yb³⁺, 2.5% Mg²⁺, 1% Nd³⁺, (e) Fe₃O₄/Gd₂O₃:1% Er³⁺, 18% Yb³⁺, 2.5% Mg²⁺, 1% Nd³⁺, (f) Fe₃O₄/Gd₂O₃:1% Er³⁺, 18% Yb³⁺, 2.5% Mg²⁺, 2% Nd³⁺, (g) Fe₃O₄/Gd₂O₃:1% Er³⁺, 18% Yb³⁺, 2.5% Mg²⁺, 4% Nd³⁺ NPs.

and 19.64 W·cm⁻²) are shown in Fig. 4(b) and SI Fig. S17(a)–(d). The area under the red luminescence curve is the largest for NPs without Nd³⁺ ions for all laser powers used, as shown in Fig. 4(c). NPs with 0% Nd³⁺ do not show luminescence at a wavelength of 560 nm. The remaining NP samples show green luminescence. The area under the green luminescence curve as a function of Nd³⁺ ion concentration is shown in SI Fig. S18. The introduction of Nd³⁺ ions did not improve the luminescence in the authors' NPs, i.e., the authors do not have spatially separated Nd³⁺ and Er³⁺ atoms. On the other hand, introducing Nd³⁺ ions with different amounts into Gd₂O₃:1% Er³⁺, 18% Yb³⁺ affects the non-radiative energy back transfer from Er³⁺ ions to Nd³⁺ ions and then influences the cross-relaxation (CR) process of Er³⁺ ions, which dominate the green-to-red emission ratio [22].

When the authors used homogeneous doping, CR from Er³⁺ to Nd³⁺ led to a decrease in upconversion upon laser excitation at a wavelength of 980 nm (as shown in Fig. 5) or 808 nm. There are three main resonant CR transitions between Nd³⁺ and Er³⁺ (purple dotted arrows) [23, 24]. Homogeneous co-doping with a high concentration of Nd³⁺ ions and activators will quench the overall upconversion emission, due to the deleterious back transfer from activators Er³⁺ to Nd³⁺ ions [25].

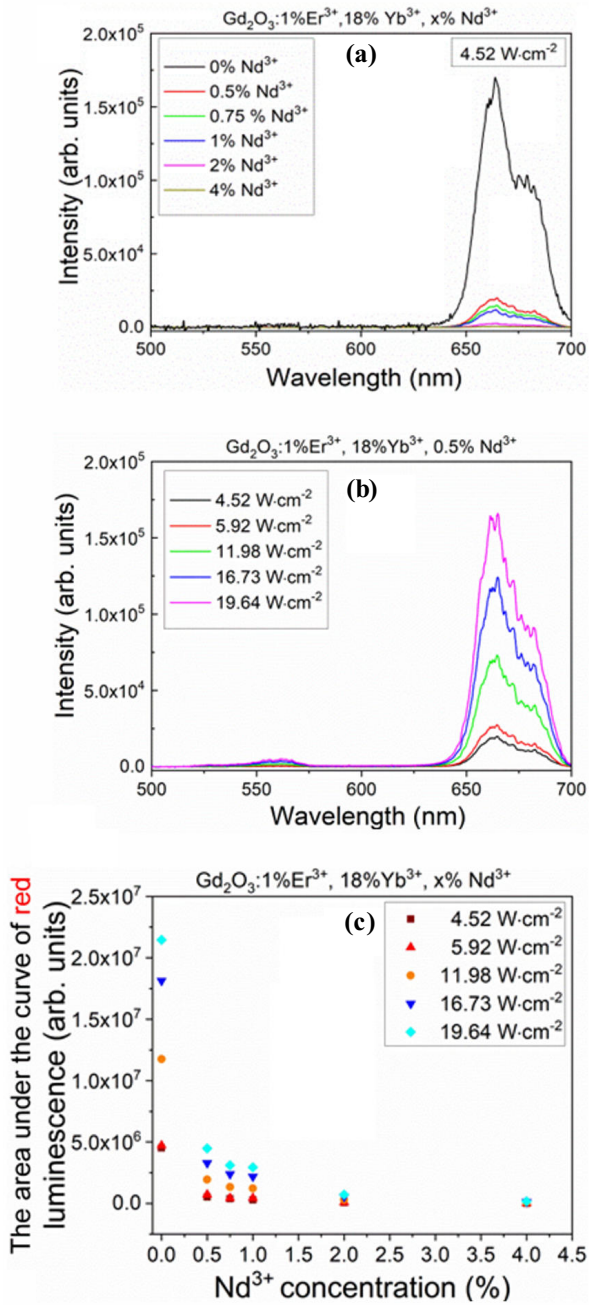


Fig. 4. (a) The PL spectra of the Gd₂O₃:1%Er³⁺, 18%Yb³⁺, x%Nd³⁺ NPs with different concentration of neodymium ions (in powder form) measured for 4.52 W·cm⁻² laser power densities for 980 nm. (b) The PL spectra of the Gd₂O₃:1%Er³⁺, 18%Yb³⁺, 0.5%Nd³⁺ NPs (in powder form) were measured for five laser power densities of 980 nm. (c) The area under the curve of red luminescence as a function of neodymium ion concentration determined for five laser power densities of 980 nm for Gd₂O₃:1%Er³⁺, 18%Yb³⁺, x%Nd³⁺ NPs.

3.2.2. Optical properties of Gd₂O₃:1%Er³⁺, 18%Yb³⁺, 2.5%Mg²⁺, x%Nd³⁺ NPs

Figure 6 and SI Fig. S19(a)–(d) demonstrate the anti-Stokes emission spectra, measured in the visible range for Gd₂O₃:1%Er³⁺, 18%Yb³⁺, 2.5%Mg²⁺, x%Nd³⁺ (x = 0.5%, 0.75%, 1%, 2%, and 4%) NPs. The luminescence of Er³⁺ ions was directly excited with a NIR light at 980 nm. The emission spectra include peaks centred at 553 nm, 564 nm, and 665 nm which is attributed to the ⁴F_{9/2}→⁴I_{15/2} and

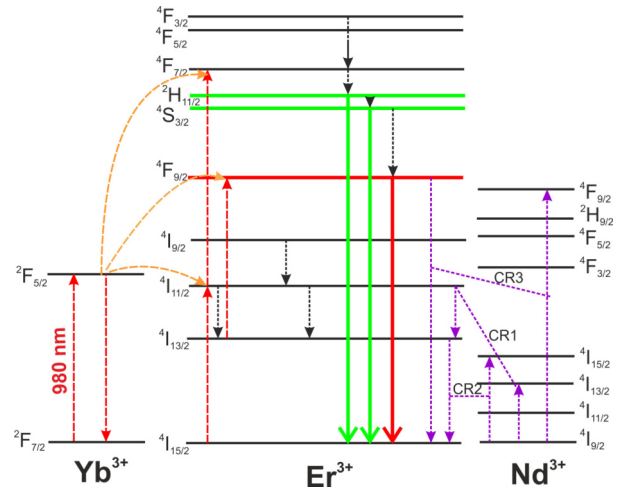


Fig. 5. The energy levels and transfers diagram for Yb³⁺, Er³⁺ and Nd³⁺ ions under the excitation with a 980 nm continuous wave laser.

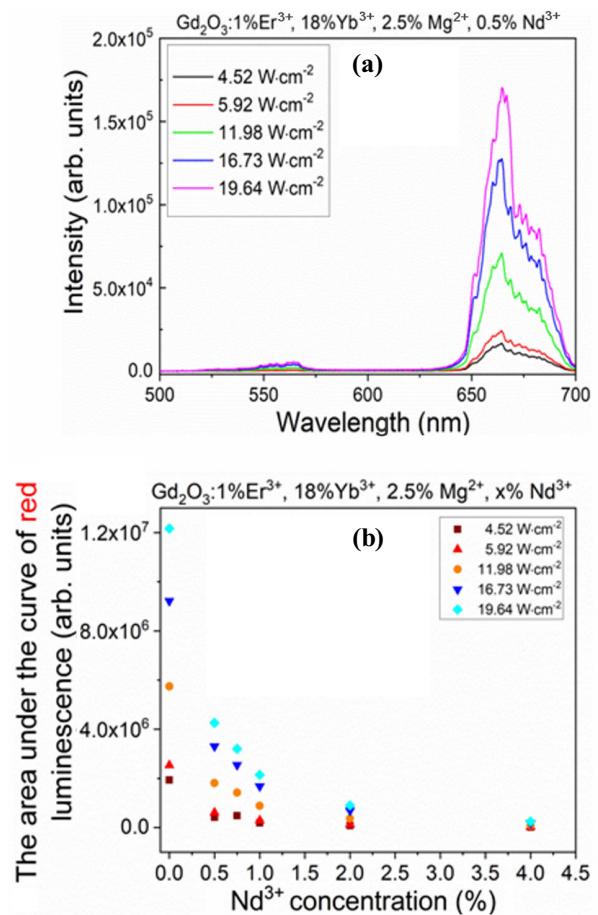


Fig. 6. The PL spectra of the Gd₂O₃:1%Er³⁺, 18%Yb³⁺, 2.5%Mg²⁺, 0.5%Nd³⁺ NPs measured for five laser power densities of 980 nm (in powder form) (a). The area under the curve of red luminescence as a function of neodymium ion concentration determined for five laser power densities of 980 nm for Gd₂O₃:1%Er³⁺, 18%Yb³⁺, 2.5%Mg²⁺, x%Nd³⁺ NPs (b).

⁴S_{3/2}→⁴I_{15/2}, ²H_{11/2}→⁴I_{15/2} in Er³⁺ ions. The PL of NPs was also measured for five 980 nm laser power densities: 4.52 W·cm⁻², 5.92 W·cm⁻², 11.98 W·cm⁻², 16.73 W·cm⁻², and 19.64 W·cm⁻². The luminescence increases with the

increase of the power density of a 980 nm laser as shown in Fig. 6(a). The area under the red luminescence curve is the largest for NPs without Nd³⁺ ions [Fig. 6(b)]. But for a 0.5% concentration of Nd³⁺ ions, the area under the curve of red luminescence is still at a relatively high level. No green luminescence was observed for NPs without Nd³⁺ ions. The largest area under the green luminescence curve was observed for the sample with 0.5% Nd³⁺ (SI Fig. S20).

3.2.3. Optical properties of Fe₃O₄/Gd₂O₃:1% Er³⁺, 18% Yb³⁺ NPs

The Fe₃O₄/Gd₂O₃:1% Er³⁺, 18% Yb³⁺ NPs with different thicknesses of the Gd₂O₃ coating: 47 nm, 95 nm, 103 nm, and 146 nm were synthesized. The NPs exhibit luminescence at a wavelength of 662 nm when excited with a NIR laser of 980 nm and five laser power densities: 4.52 W·cm⁻², 5.92 W·cm⁻², 11.98 W·cm⁻², 16.73 W·cm⁻², and 19.64 W·cm⁻² [Fig. 7(a)–(b) and SI Fig. S21(a)–(c)]. With a Gd₂O₃ coating thickness of 146 nm, they show the highest red luminescence (⁴F_{9/2}→⁴I_{15/2}) as shown in Fig. 7(b). To understand the upconversion mechanism, the upconversion emission intensity (*I*_{up}) was measured as a function of excitation power (*P*). Supporting information SI Fig. S22(a)–(d) demonstrates the dependence of *I*_{up} on *P*

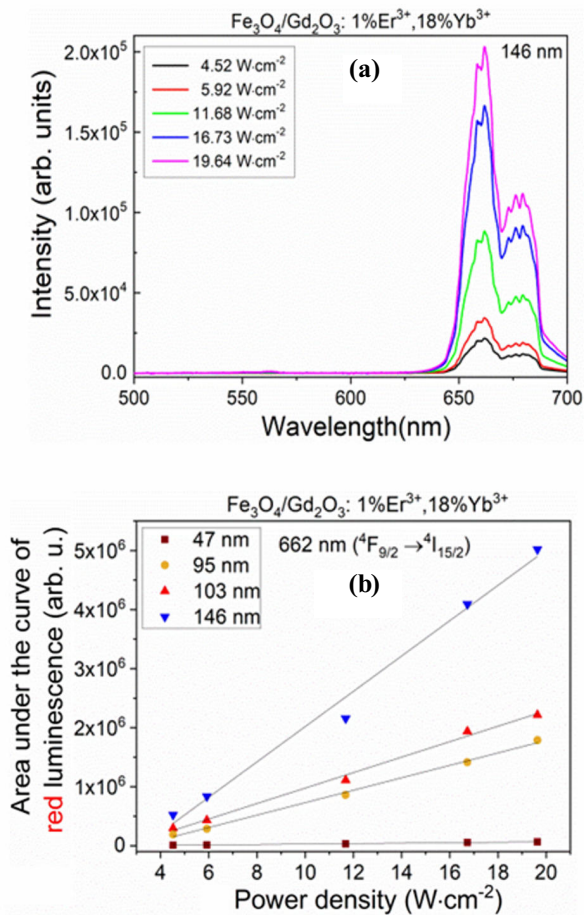


Fig. 7. The PL spectra of the Fe₃O₄/Gd₂O₃:1% Er³⁺, 18% Yb³⁺ NPs measured for five laser power densities of 980 nm, in the visible region, for a shell thickness of 146 nm (a). The area under the curve of red luminescence as a function of five laser power densities of 980 nm for Fe₃O₄/Gd₂O₃:1% Er³⁺, 18% Yb³⁺ NPs (b).

of the Fe₃O₄/Gd₂O₃:1% Er³⁺, 18% Yb³⁺ powder samples. The line of log(*I*_{up}) vs. log(*P*^{*n*}) is shown in SI Fig. S22(a)–(d). The parameter of *n* is the number of photons from the infrared region involved in generating one photon from the visible area (SI Table S3). As shown in SI Fig. S22, the *n* values calculated from the slope of the linear fit are approximately 1.47, 1.53, 1.39, and 1.53 for red luminescence at 662 nm and 1.89, 1.80, and 1.82 for green luminescence at 560 nm, respectively, indicating that the UC emission is a two-photon process.

3.2.4. Optical properties of Fe₃O₄/Gd₂O₃:1% Er³⁺, 18% Yb³⁺, 2.5% Mg²⁺, x% Nd³⁺ NPs

For the Fe₃O₄/Gd₂O₃:1% Er³⁺, 18% Yb³⁺, 2.5% Mg²⁺, x% Nd³⁺ NPs (*x* = 0%, 0.5%, 0.75%, 1%, 2%, and 4%), the NPs show emission in the visible region after excitation with a semiconductor laser with a wavelength of 980 nm as shown in Fig. 8(a)–(c), Fig. 9(a)–(d) and SI Fig. S23(a)–(d). The authors observed a significant increase in red luminescence for the Fe₃O₄/Gd₂O₃:1% Er³⁺, 18% Yb³⁺, 2.5% Mg²⁺, x% Nd³⁺ NPs in a dimethyl sulfoxide (DMSO) environment. Under these conditions, the heat dissipation is better than in the case of measurements of samples in the form of powder [26].

Spectra were collected at five laser power densities: 4.52 W·cm⁻², 5.92 W·cm⁻², 11.98 W·cm⁻², 16.73 W·cm⁻², and 19.64 W·cm⁻² [SI Fig. S24 (a)–(d)]. In this case, the luminescence increases with increasing laser power density. In the core/shell NPs adding Nd³⁺ quenches their luminescence. [Fig. 8(a) and (c)]. The area under the red luminescence curve as a function of neodymium (Nd³⁺) ion concentration in the starting solution was determined for Fe₃O₄/Gd₂O₃:1% Er³⁺, 18% Yb³⁺, 2.5% Mg²⁺, x% Nd³⁺ NPs as shown in Fig. 8(c). For other concentrations, the luminescence decreases. CR to Er³⁺ ions were also observed, as shown in Fig. 5.

The luminescence of Fe₃O₄/Gd₂O₃:1% Er³⁺, 18% Yb³⁺, 2.5% Mg²⁺, x% Nd³⁺ NPs doped with different concentrations of neodymium ions (*x* = 0%, 0.5%, 0.75%, 1%, 2%, and 4%) was investigated, when excited with a laser at a wavelength of 808 nm and a laser power density of 11.68 W·cm⁻². The NPs exhibit emission at 662 nm as shown in SI Fig. S25, which corresponds to the characteristic transitions in Er³⁺ ions. The highest luminescence is observed for 1% Nd³⁺ at an emission wavelength of 662 nm. The 662 nm emission is a superposition of two ways of erbium excitation. The first is chain excitation of neodymium ions, where the energy is transferred to ytterbium ions and, finally, as two energy transfers to erbium. The second mechanism is a ground state absorption (GSA) of 808 nm photon at Er ion, then energy transfer to Yb ion and, finally, a GSA of 808 nm photon at Er ion and energy transfer from Yb (980 nm) to the excited state of Er ion [27] can be observed.

The luminescence of Gd₂O₃:1% Er³⁺, 18% Yb³⁺, 0.5% Nd³⁺, Gd₂O₃:1% Er³⁺, 18% Yb³⁺, 2.5% Mg²⁺, 0.5% Nd³⁺ and Fe₃O₄/Gd₂O₃:1% Er³⁺, 18% Yb³⁺, 2.5% Mg²⁺, 0.5% Nd³⁺ NPs was compared in the range from 500 nm to 850 nm when excited with a semiconductor laser at a wavelength of 980 nm and a laser power density of 13.7 W·cm⁻². The highest luminescence was observed

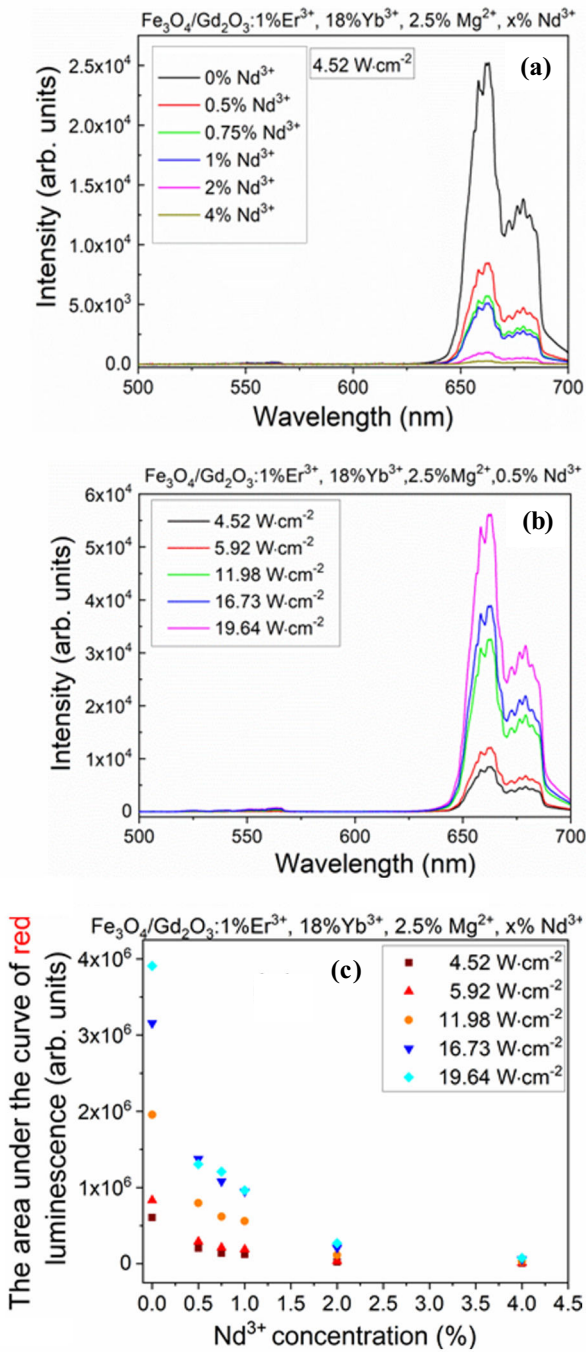


Fig. 8. (a) The PL spectra of Fe₃O₄/Gd₂O₃:1%Er³⁺, 18%Yb³⁺, 2.5%Mg²⁺, x%Nd³⁺ NPs measured for various Nd³⁺ ion concentrations for a 980 nm laser power density of 4.52 W·cm⁻². (b) PL spectra of Fe₃O₄/Gd₂O₃:1%Er³⁺, 18%Yb³⁺, 2.5%Mg²⁺, 0.5%Nd³⁺ NPs measured for five 980 nm laser power densities. (c) The area under the curves of red luminescence of core/shell NPs as a function of Nd³⁺ ion concentration determined for five different 980 nm laser power densities. Measurements were carried out for samples in the form of powder.

for magnesium-doped NPs Gd₂O₃:1%Er³⁺, 18%Yb³⁺, 2.5%Mg²⁺ at 661 nm, which corresponds to a transition in Er³⁺ ions (⁴F_{9/2}→⁴I_{15/2}) [Fig. 10(a)]. The Er³⁺ ²H_{11/2}/⁴S_{3/2}→⁴I_{13/2} transition at a wavelength of 848 nm [27] is the strongest for iron-containing NPs (Fe) Fe₃O₄/Gd₂O₃:1%Er³⁺, 18%Yb³⁺, 2.5%Mg²⁺, 0.5%Nd³⁺. The luminescence of the NPs was also measured in the infrared region from 1400 nm to 1800 nm after excitation

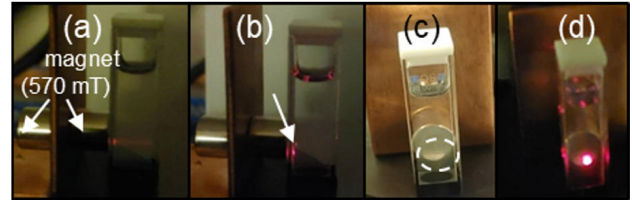


Fig. 9. The Tyndall effect of the Fe₃O₄/Gd₂O₃:1%Er³⁺, 18%Yb³⁺, 2.5%Mg²⁺, 0.5%Nd³⁺ NPs dissolved in a DMSO solution. The NPs excited with a 980 nm continuous wave laser (17.23 W·cm⁻²) (a). No Tyndall effect of the core/shell NPs attracted by a magnet (570 mT) (2 h). (b). The core/shell NPs attracted by the magnet, photo taken with the lights on (c) and excited with a wavelength of 980 nm, photo taken with the lights off (d).

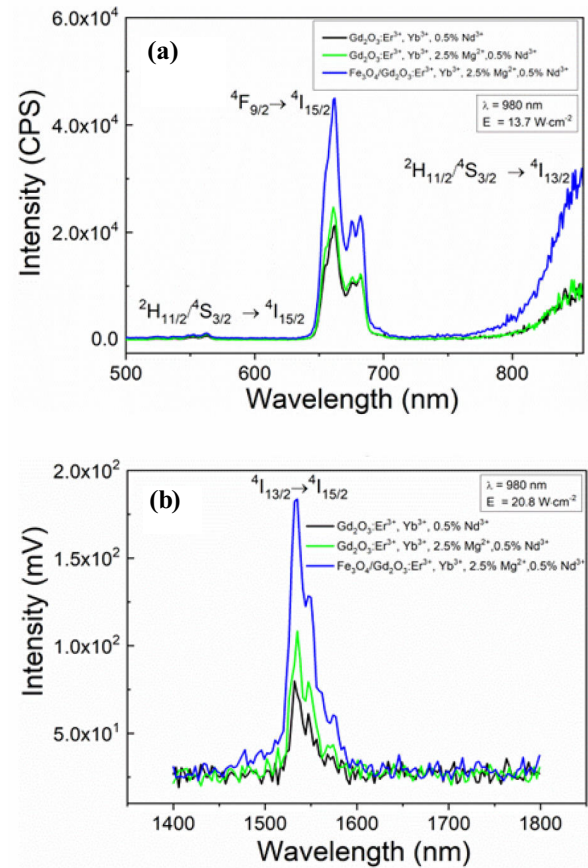


Fig. 10. Comparison of PL spectra of Gd₂O₃:1%Er³⁺, 18%Yb³⁺, 0.5%Nd³⁺; Gd₂O₃:1%Er³⁺, 18%Yb³⁺, 2.5%Mg²⁺, 0.5%Nd³⁺ and Fe₃O₄/Gd₂O₃:1%Er³⁺, 18%Yb³⁺, 2.5%Mg²⁺, 0.5%Nd³⁺ NPs in visible (a) and infrared (b) area. The NPs were excited with a semiconductor laser at a wavelength of 980 nm. The laser power densities were 13.7 W·cm⁻² and 20.8 W·cm⁻², respectively. The NPs were suspended in DMSO (concentration of 0.2 μg·ml⁻¹).

with a laser at a wavelength of 980 nm and a laser power density of 20.8 W·cm⁻². The observed luminescence is the highest for Fe₃O₄/Gd₂O₃:1%Er³⁺, 18%Yb³⁺, 2.5%Mg²⁺, 0.5%Nd³⁺ NPs as shown in Fig. 10(b). It corresponds to the transitions in Er³⁺ ⁴I_{13/2}→⁴I_{15/2}. The presence of iron causes heating of the samples.

Details regarding PL measurements of NPs are described in SI.

3.3. Magnetic properties of Fe₃O₄; Gd₂O₃:1% Er³⁺, 18% Yb³⁺; Fe₃O₄/Gd₂O₃:1% Er³⁺, 18% Yb³⁺ and Fe₃O₄/Gd₂O₃:1% Er³⁺, 18% Yb³⁺, 2.5% Mg²⁺, 0.5% Nd³⁺ NPs

Supporting information Fig. S26(a)–(b) presents the temperature dependence for the Fe₃O₄ NPs recorded in the zero-field-cooled (ZFC) and field-cooled (FC) regimes at 100 Oe. With cooling, the ZFC magnetization, M^{ZFC} , decreases, while the FC magnetization, M^{FC} , increases, but so slightly that between ~ 100 K and 5 K it appears to be temperature-independent. In the whole temperature range, the ZFC/FC curves are irreversible, therefore, it is hard to conclude about the superparamagnetic behaviour in this sample. Additionally, in the $M^{\text{ZFC}}(T)$ relation, there is no well-defined maximum that could indicate the beginning of a blocking or freezing process with the sample cooling. For the investigated Fe₃O₄ NPs, the magnetization curves, $M(H)$, were collected at 300 K and 5 K [SI Fig. S26(b)], and exhibit reversible behaviour, and a non-zero coercive field, respectively, however, their shape does not change significantly with decreasing temperature. According to the above, the investigated nano system should be treated as magnetically interacting system of NPs. Although the observation of zero coercivity at room temperature and the bifurcation of the ZFC and FC curves together with the rather small average diameter of grains (i.e., 13 nm) would suggest superparamagnetic behaviour near room temperature. Analogous ZFC-FC dependences were earlier reported in the literature on iron oxide NPs, where also the frozen state (most probably cluster-glass-like) determined by the magnetic interactions is predicted [28]. It should be noted, that the interparticle interactions are present in the investigated sample, although the non-magnetic coating on the NPs should prevent such a situation. However, in this case, the non-magnetic shell is most probably too thin or does not cover individual grains, but agglomerates of NPs, or both.

The obtained saturation magnetization, M_s , values, i.e., 74 $\text{emu}\cdot\text{g}^{-1}$ at 300 K and 84 $\text{emu}\cdot\text{g}^{-1}$ at 5 K, are lower than that predicted for bulk magnetite (98 $\text{emu}\cdot\text{g}^{-1}$ [29]), and this reduction is likely due to two reasons. The first is the mass fraction of PEG 4600 which underestimates M_s expressed in $\text{emu}\cdot\text{g}^{-1}$. The second is the NPs surface contribution, which decreases the net particle magnetic moment for ferrimagnetic NPs [30].

For Gd₂O₃:1% Er³⁺, 18% Yb³⁺ NPs, the temperature dependence of the magnetization measured at 100 Oe together with the $M(H)$ relations collected at 300 K and 5 K are plotted in SI Fig. S27(a)–(b). According to Fig. S27(a), Gd₂O₃:1% Er³⁺, 18% Yb³⁺ NPs exhibit paramagnetic behaviour in the whole temperature range used, which can be described by Curie-Weiss (C-W) model $\chi(T) = C/(T-\theta)$, where C is the Curie constant, and θ is the paramagnetic C-W temperature. (It should be added that the ZFC/FC curves registered for Gd₂O₃:1% Er³⁺, 18% Yb³⁺ coincide with each other). The C-W model was fitted to the temperature dependence of the inverse magnetic susceptibility for Gd₂O₃:1% Er³⁺, 18% Yb³⁺ [right axis in Fig. S27(b)] giving $C = 0.018$ ($\text{emu}\cdot\text{K}$)/g/Oe, and $\theta \sim -14$ K. The effective magnetic moment μ_{eff} calculated for Gd₂O₃:1% Er³⁺, 18% Yb³⁺ NPs from a relation

$$\mu_{\text{eff}} = \sqrt{\frac{3Ck_B}{N_A}}$$

(k_B and N_A are the Boltzmann constant and Avogadro number, respectively) is equal to 7.23 μ_B , thus slightly lower than the theoretical value predicted for pure Gd₂O₃, i.e., 7.94 μ_B [31]. The reduction of magnetic moment is most likely caused by Yb³⁺ impurities, the level of which is significant here (18%) and exhibits a much lower effective magnetic moment, 4.5 μ_B [32], than Gd³⁺ ions. The negative value of θ suggests the antiferromagnetic coupling between the magnetic moments of Gd³⁺ ions, which is reported frequently for Gd₂O₃ [33–36]. The paramagnetic behaviour of Gd₂O₃:1% Er³⁺, 18% Yb³⁺ NPs was also confirmed by the magnetization curves registered at 300 K and 5 K, where the linear dependence between the magnetization and H is observed [SI Fig. S27(a)]. Of note is the rapid increase of the magnetization value at 40 kOe with a decrease in temperature from 300 K to 5 K, indicating the strong fluctuations of the Gd³⁺ magnetic moment with temperature. The magnetization value registered for Gd₂O₃:1% Er³⁺, 18% Yb³⁺ at 40 kOe is equal to 77 $\text{emu}\cdot\text{g}^{-1} = 5 \mu_B$, thus it is close to the values reported in the literature for Gd₂O₃ [34, 37].

The results of temperature dependences of the magnetization measured at 100 and 500 Oe in the ZFC/FC regimes for core/shell samples with the 47 nm shell thickness are shown in SI Fig. S28(a). Both registered pairs of the ZFC and FC relations for this sample display irreversibility between 5 K and 250 K, however, their curvature is different. The curvature of the ZFC and FC dependences registered at 100 Oe is similar, i.e., during cooling, the magnetization values first increase slightly, then drop sharply and increase again between 8 K and 5 K. ZFC/FC curves measured at 500 Oe exhibit the magnetization value increase with the temperature decrease over the entire temperature range. The low-temperature increase of the magnetization value observed in the ZFC-FC relation measured at 100 Oe signifies the paramagnetic contributions from the Gd₂O₃:1% Er³⁺, 18% Yb³⁺ phase, while the broad ZFC maximum is related to the ferrimagnetic Fe₃O₄ phase. From the ZFC-FC dependence measured at 500 Oe, it can be inferred that, with increasing magnetic field value, the paramagnetic susceptibility of Gd³⁺ ions increased so significantly that it dominated the ZFC-FC dependence, despite the significant concentration of Fe₃O₄ in the sample.

The $M(H)$ relations registered at 300, 50, 10, and 5 K for the sample with a 47 nm shell (SI Fig. S28b) show a linear (paramagnetic) character with a ferrimagnetic contribution near-zero field. With the temperature decrease, the coercivity field increases from ~ 50 Oe at 300 K to ~ 320 Oe, which is consistent with the character of magnetic nanosystems, even if they are agglomerated.

The magnetization of Fe₃O₄/Gd₂O₃:1% Er³⁺, 18% Yb³⁺, 2.5% Mg²⁺, 0.5% Nd³⁺ NPs was measured as a function of the applied magnetic field at a temperature of 3 K and 300 K [SI Fig. S29(a)] and as a function of the temperature in the ZFC-FC regime, and at a magnetic field of 50 Oe [SI Fig. S29(b)]. At first glance, the results obtained for this sample are very similar to the data from Gd₂O₃:1% Er³⁺,

18% Yb³⁺, however, some differences can be distinguished, i.e., the ZFC-FC relations do not coincide perfectly, and the $M(H)$ relation measured at 3 K is not linear but slightly curved. All this means that although the dominant magnetic character of Fe₃O₄/Gd₂O₃:1% Er³⁺, 18% Yb³⁺, 2.5% Mg²⁺, 0.5% Nd³⁺ NPs is paramagnetic, the influence of ferrimagnetic Fe₃O₄ phase cannot be omitted.

Figure 11 shows the magnetization curves recorded at 300 K for three samples: Fe₃O₄; Gd₂O₃:1% Er³⁺, 18% Yb³⁺ and Fe₃O₄/Gd₂O₃:1% Er³⁺, 18% Yb³⁺, 2.5% Mg²⁺, 0.5% Nd³⁺. From the $M(H)$ dependence for the Fe₃O₄ NPs, it is possible to determine the saturation magnetization of ~74 emu·g⁻¹ and a small non-zero coercivity, which reflects the ferrimagnetic behaviour of this sample. The $M(H)$ relations obtained for the samples with Gd₂O₃ (black and red line in Fig. 11) appear to be the same, linear and overlapping. However, the magnification of the low field part of Fig. 11 signifies the well-defined paramagnetic character only for Gd₂O₃:1% Er³⁺, 18% Yb³⁺, while for Fe₃O₄/Gd₂O₃:1% Er³⁺, 18% Yb³⁺, 2.5% Mg²⁺, 0.5% Nd³⁺, the contribution of magnetite is visible as the curvature of the $M(H)$ dependence. The next stage of research will be working on increasing the volume of the core, which will have superparamagnetic properties concerning the shell with upconverting properties.

Details of the measurements determining the magnetic properties of NPs are described in SI.

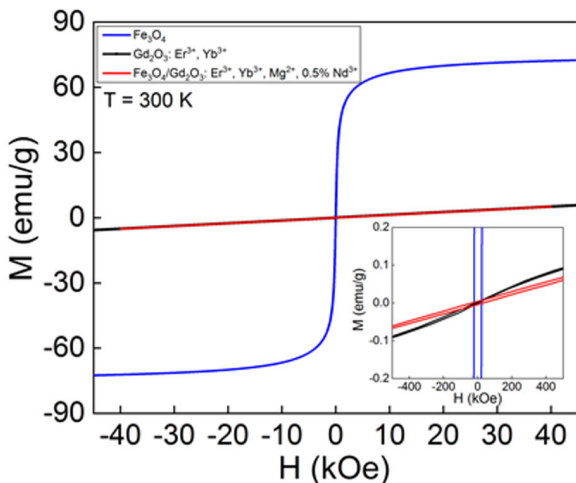


Fig. 11. Magnetization curves for three samples: Fe₃O₄; Gd₂O₃:1% Er³⁺, 18% Yb³⁺ and Fe₃O₄/Gd₂O₃:1% Er³⁺, 18% Yb³⁺, 2.5% Mg²⁺, 0.5% Nd³⁺ NPs measured at 300 K. Inset: the magnification of the central area.

3.4. PrestoBlue assay of Fe₃O₄/Gd₂O₃:1% Er³⁺, 18% Yb³⁺, 2.5% Mg²⁺, 0.5% Nd³⁺ NPs

Cytotoxicity experiments with concentrations of the Fe₃O₄/Gd₂O₃:1% Er³⁺, 18% Yb³⁺, 2.5% Mg²⁺, 0.5% Nd³⁺ NPs between 1 μg·ml⁻¹ to 1000 μg·ml⁻¹ were tested on a cell line, a human cervical carcinoma cell (HeLa) with a PrestoBlue colorimetric assay as shown in Fig. 12. The results in Fig. 12 confirmed that the hybrid Fe₃O₄/Gd₂O₃:1% Er³⁺, 18% Yb³⁺, 2.5% Mg²⁺, 0.5% Nd³⁺ are highly biocompatible at the NPs concentration up to 1000 μg·ml⁻¹ after a 24 h incubation. The observed increase in the metabolic activity of HeLa cells in the presence of NPs, compared to the control, may probably be caused by

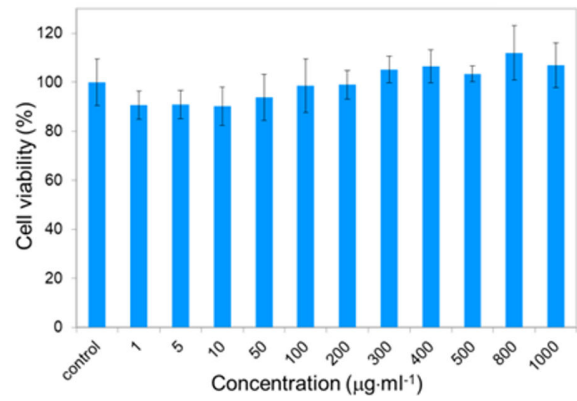


Fig. 12. Cell viability of HeLa cells after 24 h incubation with eleven concentrations of Fe₃O₄/Gd₂O₃:1% Er³⁺, 18% Yb³⁺, 2.5% Mg²⁺, 0.5% Nd³⁺ NPs as determined by PrestoBlue assay.

cellular stress. A similar increase in metabolic activity in the presence of oxide NPs was observed by other researchers. In the work of Chavez *et al.* [38], cytotoxicity tests showed that Gd₂O₃:Er³⁺/Yb³⁺ and Y₂O₃:Er³⁺/Yb³⁺ NPs in HeLa cells are non-cytotoxic. In the work of Gal *et al.* [39], a 24 h incubation of HeLa cells with PEGylated superparamagnetic iron oxide NPs of different core sizes (3–8 nm) had no significant effect on cell viability.

3.5. Confocal microscopy imaging

The obtained Fe₃O₄/Gd₂O₃:1% Er³⁺, 18% Yb³⁺, 2.5% Mg²⁺, 0.5% Nd³⁺ NPs were used as luminescent markers in HeLa tumor cells [Fig. 13(a)–(d)]. NPs with two concentrations of 25 μg·ml⁻¹ [Fig. 13(a)–(d)] and 50 μg·ml⁻¹ (SI Fig. S30) were incubated with the cells for 24 h. The luminescence spectrum of the NPs inside the cells was measured after excitation with a femtosecond laser (300 mW) as shown in Fig. 13(b).

NPs penetrate the cells by endocytosis [40, 41]. The authors performed a Z-stack scans and based on them they can conclude that the NPs are located in HeLa cancer cells (XZ and YZ cross-section), and they accumulate mainly in the cytoplasm, near the cell nucleus (SI Fig. S31). In the work of Zajdel *et al.* [42], experiments were conducted with chemical inhibitors which confirmed the involvement of endocytosis in upconverting NPs (β-NaYF₄:2.0% Yb³⁺, 2% Er³⁺) internalization and helped select several mechanisms involved in internalization.

4. Conclusions

The authors have successfully designed and synthesized novel multilayer core/shell nanostructures for upconversion applications. Optical-paramagnetic core/shell NPs were synthesized by homogeneous precipitation synthesis. The NPs show emission in the visible region (662 nm) when excited with a semiconductor laser with a wavelength of 980 nm and 808 nm. The hybrid NPs range in size from 220 nm to 641 nm, depending on the neodymium ion concentration. The produced Fe₃O₄ NPs have a cubic crystal structure (symmetry group $Fd-3m$), whereas the obtained Fe₃O₄/Gd₂O₃:1% Er³⁺, 18% Yb³⁺, 2.5% Mg²⁺, 0.5% Nd³⁺ NPs have a cubic Gd₂O₃ crystal structure (symmetry group $Ia-3$). The Fe₃O₄ NPs exhibit the

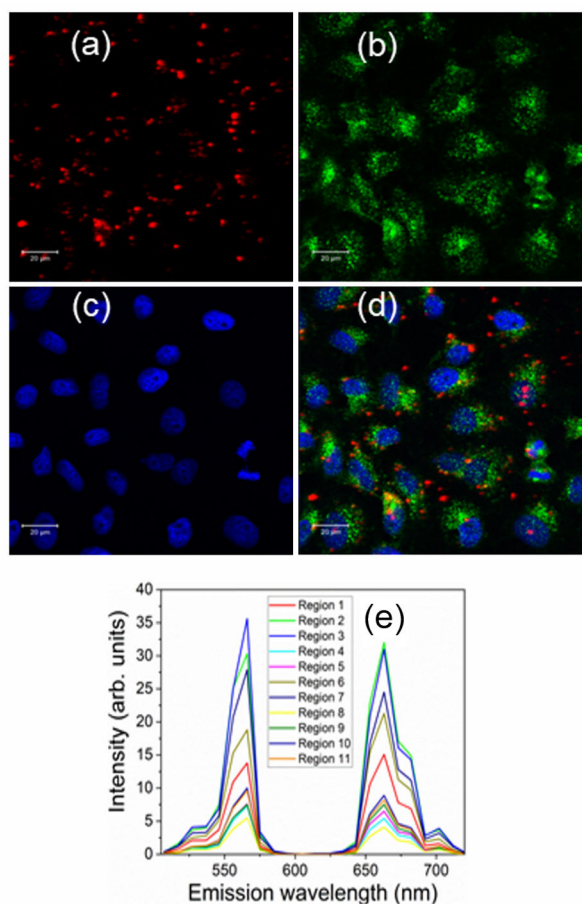


Fig. 13. Confocal image of HeLa cancer cells after a 24 h incubation in a solution with $25 \mu\text{g}\cdot\text{ml}^{-1}$ of $\text{Fe}_3\text{O}_4/\text{Gd}_2\text{O}_3:1\% \text{Er}^{3+}$, $18\% \text{Yb}^{3+}$, $2.5\% \text{Mg}^{2+}$, $0.5\% \text{Nd}^{3+}$ NPs. (a) The NPs were excited with a 980 nm femto-second laser (observed as red spots). The HeLa cells were marked using the immune-fluorescence method. (b) Antibodies conjugated with Alexa Fluor 488 dye (excited by 488 nm argon laser) were attached to the lysosomes. The signal was collected in the range from 496 nm to 570 nm (observed as green regions). (c) Nuclei stained with Hoechst 33 342 dye were excited with a wavelength of 705 nm (blue colour). The signal was collected in the range from 423 nm to 475 nm. (d) The images are a superposition of NPs luminescence, marked cell fluorescence, and nuclei fluorescence. (e) The spectra of NPs were excited by a femtosecond laser at a wavelength of 980 nm and an average laser power of 10%. Regions are placed in the confocal microscope image from which individual emission spectra of core/shell NPs were collected.

ferrimagnetic behaviour, with the saturation magnetization of $\sim 74 \text{ emu}\cdot\text{g}^{-1}$ and non-zero coercivity. The magnetic response of core/shell samples is rather paramagnetic and does not differ significantly from that registered for the shell material alone. For $\text{Gd}_2\text{O}_3:1\% \text{Er}^{3+}$, $18\% \text{Yb}^{3+}$ and $\text{Fe}_3\text{O}_4/\text{Gd}_2\text{O}_3:1\% \text{Er}^{3+}$, $18\% \text{Yb}^{3+}$, $2.5\% \text{Mg}^{2+}$, $0.5\% \text{Nd}^{3+}$, at 300 K, the values of the magnetization registered at $\sim 40 \text{ kOe}$ are similar and equal to $\sim 5.3 \text{ emu}\cdot\text{g}^{-1}$. The core/shell NPs penetrate HeLa cancer cells by endocytosis, which was confirmed by confocal microscopy studies. The NPs are non-toxic to cells up to a concentration of $1000 \mu\text{g}\cdot\text{ml}^{-1}$, which was confirmed by studies using the PrestoBlue test.

Authors' statement

Research concept and design, I.K. and K.F.; collection and/or assembly of data, I.K.; data analysis and interpretation, I.K., K.F., M.Ch., K.S., Y.Z., T.W., R.M., B.S.-D., S.L.; writing the article, I.K., K.F., M.Ch.; critical revision of the article, I.K., K.F., M.Ch.; final approval of article, I.K.

Acknowledgements

The research was funded by the Miniatura project of the National Science Centre (DEC-2022/06/X/ST5/00026). This work has been done in the NanoFun laboratories co-financed by the European Regional Development Fund within the Innovation Economy Operational Program, the project no. POIG.02.02.00-00-025/09/. The work is supported by the Foundation for Polish Science through the IRA Programme co-financed by EU within the SG OP and EFSE.

References

- [1] Kobayashi, H., Ogawa, M., Alford, R., Choyke, P. L. & Urano, Y. New strategies for fluorescent probe design in medical diagnostic imaging. *Chem. Rev.* **110**, 2620–2640 (2010). <https://doi.org/10.1021/cr900263j>
- [2] Qiu, H., Tan, M., Ohulchanskyy, T. Y., Lovell, J. F. & Chen, G. Recent progress in upconversion photodynamic therapy. *Nanomaterials* **8**, 344 (2018). <https://doi.org/10.3390/nano8050344>
- [3] Shabanzadeh-Kouyakh, A., Masoudi, A. & Ardestani, M. Synthesis method of novel $\text{Gd}_2\text{O}_3@/\text{Fe}_3\text{O}_4$ nanocomposite modified by dextrose capping agent. *Ceram. Int.* **9**, 13442–13448 (2020). <https://doi.org/10.1016/j.ceramint.2020.02.127>
- [4] Qin, M. et al. Uniform $\text{Fe}_3\text{O}_4/\text{Gd}_2\text{O}_3$ -DHCA nanocubes for dual-mode MR imaging. *Beilstein J. Nanotechnol.* **11**, 1000–1009 (2020). <https://doi.org/10.3762/bjnano.11.84>
- [5] Tan, J., Shah, S., Thomas, A., Ou-Yang, H. D. & Liu, Y. The influence of size, shape and vessel geometry on nanoparticle distribution. *Microfluid. Nanofluidics* **14**, 77–87 (2013). <https://doi.org/10.1007/s10404-012-1024-5>
- [6] Peng, H., Cui, B. & Wang, Y. Bifunctional $\text{Fe}_3\text{O}_4@/\text{Gd}_2\text{O}_3:\text{Eu}^{3+}$ nanocomposites obtained by the homogeneous precipitation method. *Mat. Res. Bull.* **48**, 1767–1771 (2013). <https://doi.org/10.1016/j.materresbull.2013.01.001>
- [7] Shabanzadeh-Kouyakh, A. Embedding Gd_2O_3 nanoparticles hydrothermally prepared in a Fe_3O_4 shell and surface modification with a dextrose bio capping agent. *Ceram. Int.* **48**, 31326–31333 (2022). <https://doi.org/10.1016/j.ceramint.2022.06.285>
- [8] Chame, K. F. et al. Green and red upconversion luminescence in multifunctional $\text{Ag}@/\text{Fe}_3\text{O}_4@/\text{Gd}_2\text{O}_3:\text{Er}^{3+}$ composites. *J. Alloys Compd.* **744**, 683–690 (2018). <https://doi.org/10.1016/j.jallcom.2018.02.038>
- [9] Shen, J., Sun, L.-D., Zhang, Y.-W. & Yan, Ch.-H. Superparamagnetic and upconversion emitting $\text{Fe}_3\text{O}_4/\text{NaYF}_4:\text{Yb}$, Er heteronanoparticles via a crosslinker anchoring strategy. *Chem. Commun.* **46**, 5731–5733 (2010). <https://doi.org/10.1039/C0CC00814A>
- [10] Tejada, E. M., Arámburo, M., Vargas, E., Contreras, O. E. & Hirata, G. A. Novel bifunctional $\text{Nd}:\text{YAG}/\text{Fe}_3\text{O}_4$ nanocomposite as nanothermometer/nanoheater for potential biomedical applications. *J. Phys. D: Appl. Phys.* **51**, 40LT01 (2018). <https://iopscience.iop.org/article/10.1088/1361-6463/aaad7e5>
- [11] Jing, P. et al. Controlled fabrication of bi-functional $\text{Fe}_3\text{O}_4@/\text{SiO}_2@/\text{Gd}_2\text{O}_3:\text{Yb}$, Er nanoparticles and their magnetic, up-conversion luminescent properties. *RSC Adv.* **4**, 44575 (2014). <https://doi.org/10.1039/C4RA06146B>
- [12] Vu, H. H. T., Atabaev, T. Sh., Nguyen, N. D., Hwang, Y.-H. & Kim, H.-K. Luminescent core-shell $\text{Fe}_3\text{O}_4@/\text{Gd}_2\text{O}_3:\text{Er}^{3+}$, Li^+ composite particles with enhanced optical properties. *J. Sol-Gel Sci. Technol.*

- 71, 391–395 (2014).
<https://doi.org/10.1007/s10971-014-3382-9>
- [13] Wu, T. *et al.* Effect of solution pH value changes on fluorescence intensity of magnetic-luminescent $\text{Fe}_3\text{O}_4/\text{Gd}_2\text{O}_3:\text{Eu}^{3+}$ nanoparticles. *J. Rare Earths* **34**, 71–76 (2016).
[https://doi.org/10.1016/S1002-0721\(14\)60581-0](https://doi.org/10.1016/S1002-0721(14)60581-0)
- [14] Yadaw, P. K., Padhi, R. K., Dubey, V., Rao, M. C. & Swamy, N. K. Influence of excitation wavelength on the down-conversion photoluminescence characteristics of $\text{Gd}_2\text{O}_3:\text{Er}^{3+}-\text{Yb}^{3+}$ phosphor. *Inorg. Chem. Commun.* **143**, 109736 (2022).
<https://doi.org/10.1016/j.inoche.2022.109736>
- [15] Priya, R., Pandey, O. P. & Dhoble, S. J. Review on the synthesis, structural and photo-physical properties of Gd_2O_3 phosphors for various luminescent applications. *Opt. Laser Technol.* **135**, 106663 (2021). <https://doi.org/10.1016/j.optlastec.2020.106663>
- [16] Kamińska, I. *et al.* Synthesis and characterization of $\text{Gd}_2\text{O}_3:\text{Er}^{3+}, \text{Yb}^{3+}$ doped with $\text{Mg}^{2+}, \text{Li}^+$ ions—effect on the photoluminescence and biological applications. *Nanotechnology* **32**, 245705 (2021).
<https://iopscience.iop.org/article/10.1088/1361-6528/abed02>
- [17] Liu, B., Li, C., Yang, P., Hou, Z. & Lin, J. 808-nm-light-excited lanthanide-doped nanoparticles: rational design, luminescence control and theranostic applications. *Adv. Mater.* **29**, 1605434 (2017). <https://doi.org/10.1002/adma.201605434>
- [18] Gao, Y., Murai, S., Shinozaki, K. & Tanaka, K. Up-conversion luminescence enhanced by the plasmonic lattice resonating at the transparent window of water. *ACS Appl. Energy Mater.* **4**, 2999–3007 (2021). <https://doi.org/10.1021/acsaem.0c01826>
- [19] Kushida, T., Marcos, H. M. & Geusic, J. E. Laser transition cross section and fluorescence branching ratio for Nd^{3+} in yttrium aluminum garnet. *Phys. Rev.* **167**, 289–291 (1968).
<https://doi.org/10.1103/PhysRev.167.289>
- [20] Liégard, F., Doualan, J. L., Moncorgé, R. & Bettinelli, M. $\text{Nd}^{3+} \rightarrow \text{Yb}^{3+}$ energy transfer in a codoped metaphosphate glass as a model for Yb^{3+} laser operation around 980 nm. *Appl. Phys. B* **80**, 985–991 (2005). <https://doi.org/10.1007/s00340-005-1829-y>
- [21] Shen, S. *et al.* Magnetic nanoparticle clusters for photothermal therapy with near-infrared irradiation. *Biomaterials* **39**, 67–74 (2015). <https://doi.org/10.1016/j.biomaterials.2014.10.064>
- [22] Meza, O., Diaz-Torres, L. A., Salas, P., de la Rosa, E. & Solis, D. Color tunability of the upconversion emission in Er-Yb doped the wide band gap nanophosphors ZrO_2 and Y_2O_3 . *Mater. Sci. Eng. B* **174**, 177–181 (2010). <https://doi.org/10.1016/j.mseb.2010.03.015>
- [23] Tian, L. *et al.* The upconversion luminescence of $\text{Er}^{3+}/\text{Yb}^{3+}/\text{Nd}^{3+}$ triply-doped $\beta\text{-NaYF}_4$ nanocrystals under 808-nm excitation. *Materials* **7**, 7289–7303 (2014). <https://doi.org/10.3390/ma7117289>
- [24] Zhao, X. *et al.* Controlling the multicolor upconversion luminescence in CaF_2 nanocrystals doped with $\text{Yb}^{3+}, \text{Er}^{3+}$ and Nd^{3+} ions under the excitation of a 808 nm laser. *Opt. Mater. Express* **9**, 4578–4587 (2019). <https://doi.org/10.1364/OME.9.004578>
- [25] Wen, S. *et al.* Advances in highly doped upconversion nanoparticles. *Nat. Commun.* **9**, 2415 (2018).
<https://doi.org/10.1038/s41467-018-04813-5>
- [26] Kamińska, I. *et al.* Upconverting/magnetic: $\text{Gd}_2\text{O}_3: (\text{Er}^{3+}, \text{Yb}^{3+}, \text{Zn}^{2+})$ nanoparticles for biological applications: effect of Zn^{2+} doping. *RSC Adv.* **5**, 78361 (2015).
<https://doi.org/10.1039/C5RA11888C>
- [27] Wanga, H. *et al.* Luminescence property tuning of $\text{Yb}^{3+}-\text{Er}^{3+}$ doped oxysulfide using multiple-band co-excitation. *RSC Adv.* **8**, 16557–1656 (2018). <https://doi.org/10.1039/C8RA02503G>
- [28] Pacakova, B., Kubickova, S., Reznickova, A., Niznansky, D. & Vejpravova, J. Spinel Ferrite Nanoparticles: Correlation of Structure and Magnetism. in *Magnetic Spinels – Synthesis, Properties and Applications* (ed. Seehra, M. S.) ch. 1 (IntechOpen, 2017).
<https://doi.org/10.5772/66074>
- [29] Chikazumi, S. & Graham, C. D. *Physics of Ferromagnetism*. (Oxford Science Publications, 1997).
- [30] Knobel, M. *et al.* Superparamagnetism and other magnetic features in granular materials: A review on ideal and real systems. *J. Nanosci. Nanotechnol.* **8**, 2836–2857 (2008).
<https://doi.org/10.1166/jnn.2008.15348>
- [31] Fukuma, K. & Torii, M. Absolute calibration of low- and high-field magnetic susceptibilities using rare earth oxides. *Geochem. Geophys. Geosyst.* **12**, 1–11 (2011).
<https://doi.org/10.1029/2011GC003694>
- [32] Cao, S. *et al.* Electronic structure and direct observation of ferrimagnetism in multiferroic hexagonal YbFeO_3 . *Phys. Rev. B* **95**, 224428 (2017). <https://doi.org/10.1103/PhysRevB.95.224428>
- [33] Foex, G. Selected constants of diamagnetism and paramagnetism. in *Tables of Constants and Numerical Data 5–226* (Allard, S. & Masson, Paris, 1957).
- [34] Hacker, H., Lin, M. S. & Westrum Jr., E. F. Magnetic Susceptibility of Several Rare Earth Oxides. in *3rd Conference on Rare Earth Research* 93–105 (Gordon and Breach, New York, 1963).
- [35] Correa, E. L. *et al.* Properties of Gd_2O_3 nanoparticles studied by hyperfine interactions and magnetization measurements. *AIP Adv.* **6**, 056112 (2016). <https://doi.org/10.1063/1.4943601>
- [36] Žid, L., Zelenák, V., Berkutova, A., Szűcsóvá, J. & Zelenáková, A. Nanocargo-delivery platform for targeted drug delivery in biomedical applications: Magnetic Gd_2O_3 nanoparticles in porous SiO_2 . *Acta Phys. Pol. A* **137**, 773–775 (2020).
<https://doi.org/10.12693/APhysPolA.137.773>
- [37] Hazarika, S. *et al.* Magnetic and magnetocaloric properties of rare-earth substituted Gd_2O_3 nanorods. *AIP Adv.* **12**, 035208 (2022).
<https://doi.org/10.1063/9.0000278>
- [38] Chavez, D. H., Juarez-Moreno, K. & Hirata, G. A. Aminosilane functionalization and cytotoxicity effects of upconversion nanoparticles Y_2O_3 and Gd_2O_3 Co-doped with Yb^{3+} and Er^{3+} . *Nanobiomedicine* **2016**, 1–7 (2016). <https://doi.org/10.5772/62252>
- [39] Gal, N. *et al.* Interaction of size-tailored pegylated iron oxide nanoparticles with lipid membranes and cells. *ACS Biomater. Sci. Eng.* **3**, 249–259 (2017).
<https://doi.org/10.1021/acsbomaterials.6b00311>
- [40] Kamińska, I. *et al.* Synthesis of $\text{ZnAl}_2\text{O}_4: (\text{Er}^{3+}, \text{Yb}^{3+})$ spinel-type nanocrystalline upconverting luminescent marker in HeLa carcinoma cells, using a combustion aerosol method route. *RSC Adv.* **4**, 56596 (2014). <https://doi.org/10.1039/C4RA10976G>
- [41] Kamińska, I. *et al.* Synthesis and characterization of $\text{Gd}_2\text{O}_3:\text{Er}^{3+}, \text{Yb}^{3+}$ doped with $\text{Mg}^{2+}, \text{Li}^+$ ions—effect on the photoluminescence and biological applications. *Nanotechnology* **32**, 245705 (2021).
<https://doi.org/10.1088/1361-6528/abed02>
- [42] Zajdel, K. *et al.* Nano-bio interactions of upconversion nanoparticles at subcellular level: biodistribution and cytotoxicity. *Nanomedicine* **18**, 233–258 (2023). <https://doi.org/10.2217/nmm-2022-0320>

Supporting Information:

Photoluminescence (PL) of the NPs

The photoluminescence (PL) spectra in the visible (VIS) region were measured with a Jobin-Yvon SPEX 270M monochromator equipped with liquid-nitrogen-cooled CCD matrix (Si). The excitation source ($\lambda_{exc} = 980$ nm) was an MDL-N-980-8W infrared (IR) laser diode and an 808 nm excitation source was a TCLDM9 (Thorlabs) equipped with a LDC220C laser diode controller and a TED200C temperature controller. For the measurement of PL in the VIS region from 500 nm to 700 nm, a Shortpass Filter FES0700 (Thorlabs) was used.

PL spectra in the VIS area from 500 nm to 850 nm and IR area from 1400 nm to 1800 nm were measured at room temperature using a Horiba/Jobin-Yvon Fluorolog-3 spectrofluorometer with a 980 nm semiconductor laser as an excitation source. Optical detection was performed with a Hamamatsu R928P PMT detector (250–850 nm) in the photon counting mode or a cooled PBS solid-state detector (900–3000 nm). The PL spectra were corrected for the spectral response of the spectrometer system used.

Powder X-ray diffraction

X-ray diffraction was applied for the evaluation of Fe_3O_4 , $\text{Gd}_2\text{O}_3:(\text{Er}, \text{Yb}, \text{Mg}, \text{Nd})$ and $\text{Fe}_3\text{O}_4/\text{Gd}_2\text{O}_3:(\text{Er}, \text{Yb}, \text{Mg}, \text{Nd})$ NPs (powdered) crystal structure and size. NPs were investigated using a Philips X'Pert Pro Alpha1 MPD diffractometer (Panalytical) ($\lambda = 1.5406$ Å).

Transmission Electron Microscopy (TEM)

Structure and morphology measurements of obtained Fe_3O_4 , $\text{Gd}_2\text{O}_3:(\text{Er}, \text{Yb}, \text{Mg}, \text{Nd})$ and $\text{Fe}_3\text{O}_4/\text{Gd}_2\text{O}_3:(\text{Er}, \text{Yb}, \text{Mg}, \text{Nd})$ NPs were performed on a transmission electron microscopy (TEM) Talos F200X (FEI) microscope operating at a maximum accelerating voltage of 200 kV. A small amount of sonicated NPs suspended in ethanol was applied on the surface of an amorphous carbon film deposited on a copper mesh. After the complete evaporation of ethanol, the grid was placed in the microscope chamber. Selected NPs were studied in three imaging modes: in bright field, dark field, and high-resolution microscopy. Energy-dispersive X-ray spectroscopy is used to make maps of elements building NPs.

Scanning Electron Microscopy (SEM) imaging

Morphology and composition measurement of synthesized Fe_3O_4 , $\text{Gd}_2\text{O}_3:(\text{Er}, \text{Yb}, \text{Mg}, \text{Nd})$, and $\text{Fe}_3\text{O}_4/\text{Gd}_2\text{O}_3:(\text{Er}, \text{Yb}, \text{Mg}, \text{Nd})$ NPs were carried out on a high-resolution SEM-Auriga microscope (Carl Zeiss) operating in the accelerating voltage range from 1 kV to 5 kV.

Magnetic properties of the NPs

The magnetic measurements were performed using a commercial physical property measurement system (PPMS, Quantum Design) equipped with an AC Measurement System (ACMS) and vibrating sample magnetometer (VSM) options. Using the VSM option, temperature dependences of the dc magnetization were collected in the zero-field-cooled (ZFC) and field-cooled (FC) regimes in the stable magnetic field $H = 100$ Oe, and in the range from 5 K to 350 K, as well as magnetization curves at 5 K and 300 K were collected, and for selected samples at several temperatures between these values. Additionally, for the sample with a 47 nm shell, the ZFC-FC curves were measured for the higher magnetic field which equals 500 Oe. AC magnetic susceptibility was measured only for the sample with a 47 nm shell – temperature dependences of the real, $\text{Re}\chi(T)$, and imaginary part, $\text{Im}\chi(T)$, of magnetic susceptibility were recorded between 5 K and 300 K at several frequencies of the alternating magnetic field in the range from 70 Hz to 10 kHz, with an amplitude equal to 4 Oe.

Confocal microscopy

The HeLa cells were cultured in Dulbecco-modified Eagle medium (DMEM) containing 10% fetal bovine serum (FBS) and 1% antibiotics (penicillin, streptomycin). Cultures of cells were incubated at 37 °C in an atmosphere containing 5% CO_2 . Cells were cultured in 6 well plates ($6 \cdot 10$ cm²) containing coverslips at a density of 10^5 /plate. After 24 h, the culture medium was removed and 2 ml of solutions with $25 \mu\text{g} \cdot \text{ml}^{-1}$ and $50 \mu\text{g} \cdot \text{ml}^{-1}$ of NPs in DMEM were added. Cells were incubated with NPs for 24 h. After this time, the cells were washed twice with PBS to remove residual NPs outside the cells and then fixed with 3.7% formaldehyde in PBS for 20 min. Next, the permeabilization of cell membranes with 2 ml of a 1% solution of TritonX-100 in 5% FBS in PBS for 10 min was done. Then, permeabilization was blocked for 30 min in 5% FBS in PBS. The cells were then incubated with primary rabbit polyclonal antibody against LAMP1 (lysosome marker) (25 μl of the antibody in 5% FBS in PBS was added to the cells and incubated for 1 h). Next, the cells were washed with PBS and goat secondary antibody to Rabbit IgG conjugated with Alexa Fluor 488 was connected to the primary antibody. The procedure was the same as the previous one. The nucleus was stained by adding 25 μl of Hoechst 33 342 and left for 10 min. Afterward, the cells were washed with PBS and were applied to a microscopic slide.

Bioimaging of HeLa cells, incubated with the $\text{Fe}_3\text{O}_4/\text{Gd}_2\text{O}_3:1\% \text{Er}^{3+}, 18\% \text{Yb}^{3+}, 2.5\% \text{Mg}^{2+}, 0.5\% \text{Nd}^{3+}$ NPs, was performed using a commercial confocal laser scanning microscope (Zeiss 710 NLO) with a NIR femtosecond laser (Coherent, Chameleon). The samples were excited by 980 nm, and UC visible emission channels were detected at 500 nm to 721 nm. Antibodies conjugated with Alexa Fluor 488 dye (excited by 488 nm argon laser) were attached to the lysosomes. The signal was collected in the range from 496 nm to 570 nm (observed as a green region). Nuclei stained with Hoechst 33 342 dye were excited with a wavelength of 705 nm (blue colour). The signal was collected in the range from 423 nm to 475 nm.

PrestoBlue assay of $\text{Fe}_3\text{O}_4/\text{Gd}_2\text{O}_3:1\% \text{Er}^{3+}, 18\% \text{Yb}^{3+}, 2.5\% \text{Mg}^{2+}, 0.5\% \text{Nd}^{3+}$ NPs

For viability testing, cells were placed in a 96-well plate at 10 000 cells per well and left overnight in an incubator (37 °C and 5% CO_2 in the atmosphere). After 24 h, the medium was removed and fresh medium containing NPs at the appropriate concentration (1, 5, 10, 50, 100, 200, 300, 400, 500, 800, 1000 $\mu\text{g}\cdot\text{ml}^{-1}$) was added. The activity was performed in four replications. Cells with the medium with NPs were placed in an incubator for 24 h. After the incubation time, the medium with NPs was removed and the cells were washed with PBS buffer to remove NPs that did not penetrate the cells. For the PrestoBlue test, the cells were flooded with a medium mixture containing 10% PrestoBlue reagent and incubated for 1 h, and then the plate was read by measuring its fluorescence at 520 nm excitation and 580 nm emission.

Table S1.
Summary of the obtained materials.

	Urea $\text{CO}(\text{NH}_2)_2$ (g)	Gadolinium nitrate $\text{Gd}(\text{NO}_3)_3 \cdot 6\text{H}_2\text{O}$ (g)	Erbium nitrate $\text{Er}(\text{NO}_3)_3 \cdot 5\text{H}_2\text{O}$ (mg)	Ytterbium nitrate $\text{Yb}(\text{NO}_3)_3 \cdot 5\text{H}_2\text{O}$ (g)	Neodymium nitrate $\text{Nd}(\text{NO}_3)_3 \cdot 6\text{H}_2\text{O}$ (g)	Magnesium nitrate $\text{Mg}(\text{NO}_3)_2 \cdot 6\text{H}_2\text{O}$ (g)
$\text{Gd}_2\text{O}_3:1\% \text{Er}^{3+}, 18\% \text{Yb}^{3+}$	25.4	7.64	44.9	0.8	–	–
$\text{Gd}_2\text{O}_3:1\% \text{Er}^{3+}, 18\% \text{Yb}^{3+}, 2.5\% \text{Mg}^{2+}$	25.4	7.64	44.9	0.8	–	0.064
$\text{Gd}_2\text{O}_3:1\% \text{Er}^{3+}, 18\% \text{Yb}^{3+}, 0.5\% \text{Nd}^{3+}$	25.4	7.64	44.9	0.8	0.02	–
$\text{Gd}_2\text{O}_3:1\% \text{Er}^{3+}, 18\% \text{Yb}^{3+}, 0.75\% \text{Nd}^{3+}$	25.4	7.64	44.9	0.8	0.03	–
$\text{Gd}_2\text{O}_3:1\% \text{Er}^{3+}, 18\% \text{Yb}^{3+}, 1\% \text{Nd}^{3+}$	25.4	7.64	44.9	0.8	0.04	–
$\text{Gd}_2\text{O}_3:1\% \text{Er}^{3+}, 18\% \text{Yb}^{3+}, 2\% \text{Nd}^{3+}$	25.4	7.64	44.9	0.8	0.08	–
$\text{Gd}_2\text{O}_3:1\% \text{Er}^{3+}, 18\% \text{Yb}^{3+}, 4\% \text{Nd}^{3+}$	25.4	7.64	44.9	0.8	0.17	–
$\text{Gd}_2\text{O}_3:1\% \text{Er}^{3+}, 18\% \text{Yb}^{3+}, 2.5\% \text{Mg}^{2+}, 0.5\% \text{Nd}^{3+}$	25.4	7.64	44.9	0.8	0.02	0.064
$\text{Gd}_2\text{O}_3:1\% \text{Er}^{3+}, 18\% \text{Yb}^{3+}, 2.5\% \text{Mg}^{2+}, 0.75\% \text{Nd}^{3+}$	25.4	7.64	44.9	0.8	0.03	0.064
$\text{Gd}_2\text{O}_3:1\% \text{Er}^{3+}, 18\% \text{Yb}^{3+}, 2.5\% \text{Mg}^{2+}, 1\% \text{Nd}^{3+}$	25.4	7.64	44.9	0.8	0.04	0.064
$\text{Gd}_2\text{O}_3:1\% \text{Er}^{3+}, 18\% \text{Yb}^{3+}, 2.5\% \text{Mg}^{2+}, 2\% \text{Nd}^{3+}$	25.4	7.64	44.9	0.8	0.08	0.064
$\text{Gd}_2\text{O}_3:1\% \text{Er}^{3+}, 18\% \text{Yb}^{3+}, 2.5\% \text{Mg}^{2+}, 4\% \text{Nd}^{3+}$	25.4	7.64	44.9	0.8	0.17	0.064

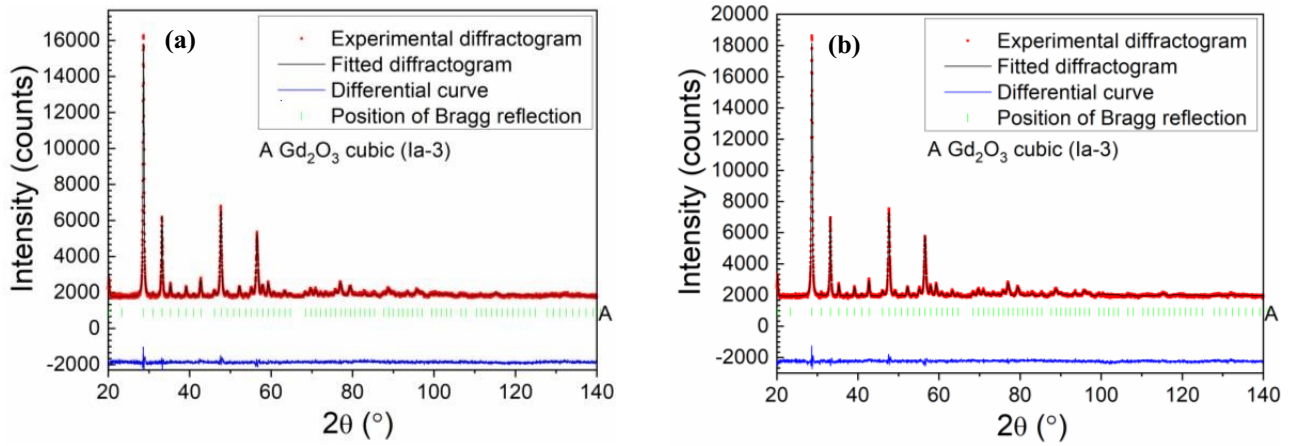


Fig. S1. Experimental X-ray diffractograms measured (a) for $\text{Gd}_2\text{O}_3:1\% \text{Er}^{3+}, 18\% \text{Yb}^{3+}, 0.5\% \text{Nd}^{3+}$; (b) $\text{Gd}_2\text{O}_3:1\% \text{Er}^{3+}, 18\% \text{Yb}^{3+}, 2.5\% \text{Mg}^{2+}, 0.5\% \text{Nd}^{3+}$ NPs and matched by the means of the Rietveld method theoretical diffractograms. Symbols: (•) experimental and (—) fitted diffractograms, (—) differential curve, and (|) positions of Bragg reflections (coming from the Gd_2O_3 phase).

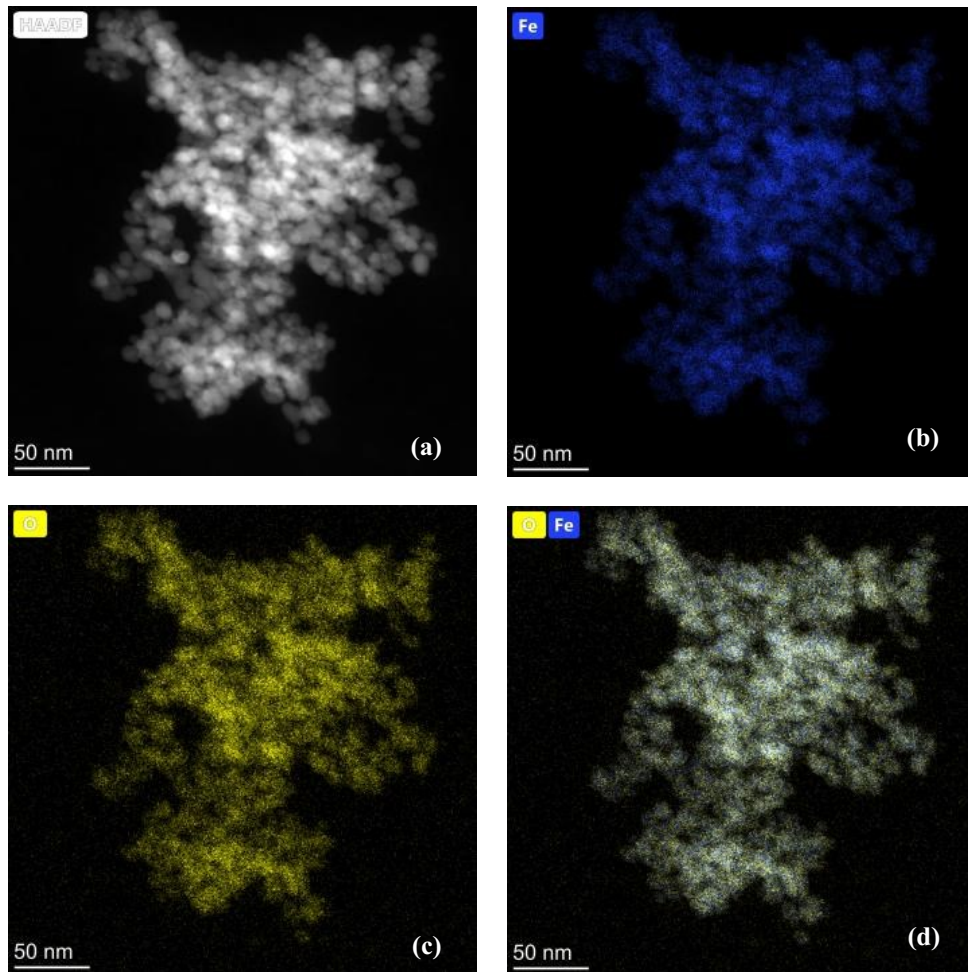


Fig. S2. TEM elements distribution maps of Fe_3O_4 NPs: (a) HAADF image, (b) Fe, (c) O, and (d) O and Fe.

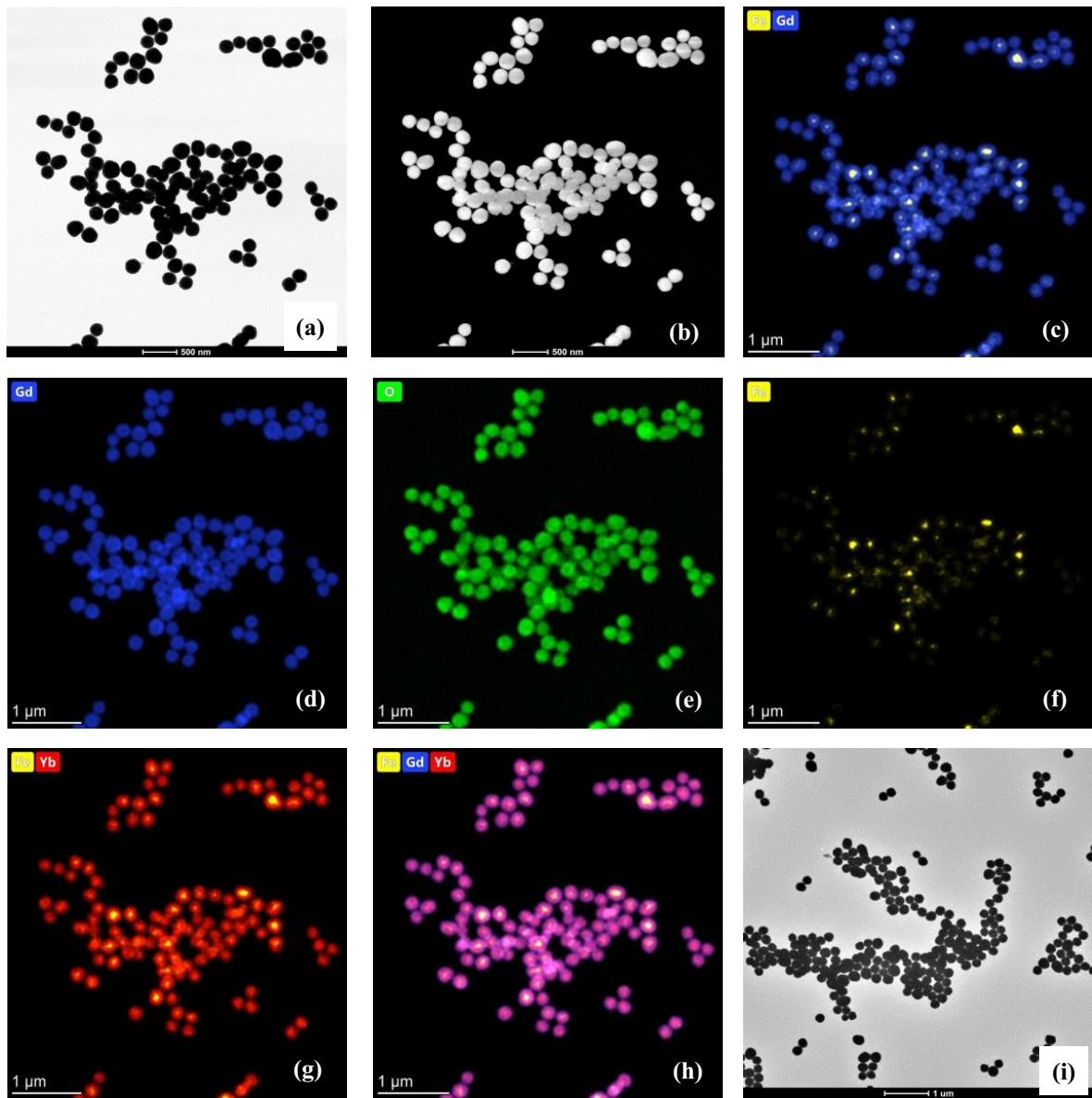


Fig. S3. TEM images of $\text{Fe}_3\text{O}_4/\text{Gd}_2\text{O}_3:1\% \text{Er}^{3+}$, $18\% \text{Yb}^{3+}$, $2.5\% \text{Mg}^{2+}$, $0.5\% \text{Nd}^{3+}$ NPs in bright (a) and dark field (b). The distribution maps of the above-mentioned elements of the NPs Fe and Gd (c), Gd (d), O (e), Fe (f), Fe and Yb (g), Fe, Gd, and Yb (h), TEM image of the NPs (i).

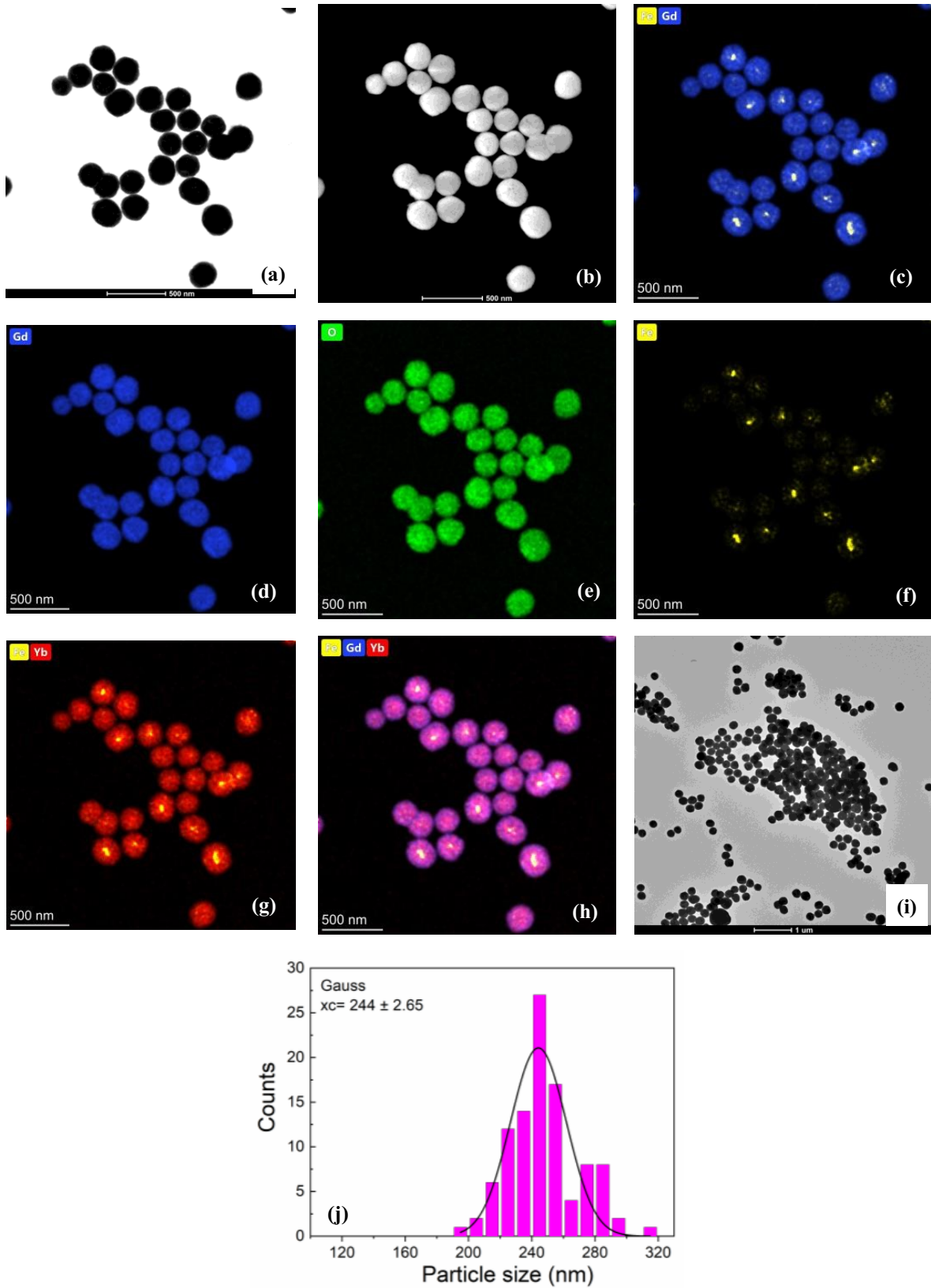


Fig. S4. TEM images of Fe₃O₄/Gd₂O₃:1% Er³⁺, 18% Yb³⁺, 2.5% Mg²⁺, 0.75% Nd³⁺ NPs in bright (a) and dark field (b). The distribution maps of the above-mentioned elements of the NPs Fe and Gd (c), Gd (d), O (e), Fe (f), Fe and Yb (g), Fe, Gd, and Yb (h), TEM image of the NPs (i). Histogram of NP size distribution (j).

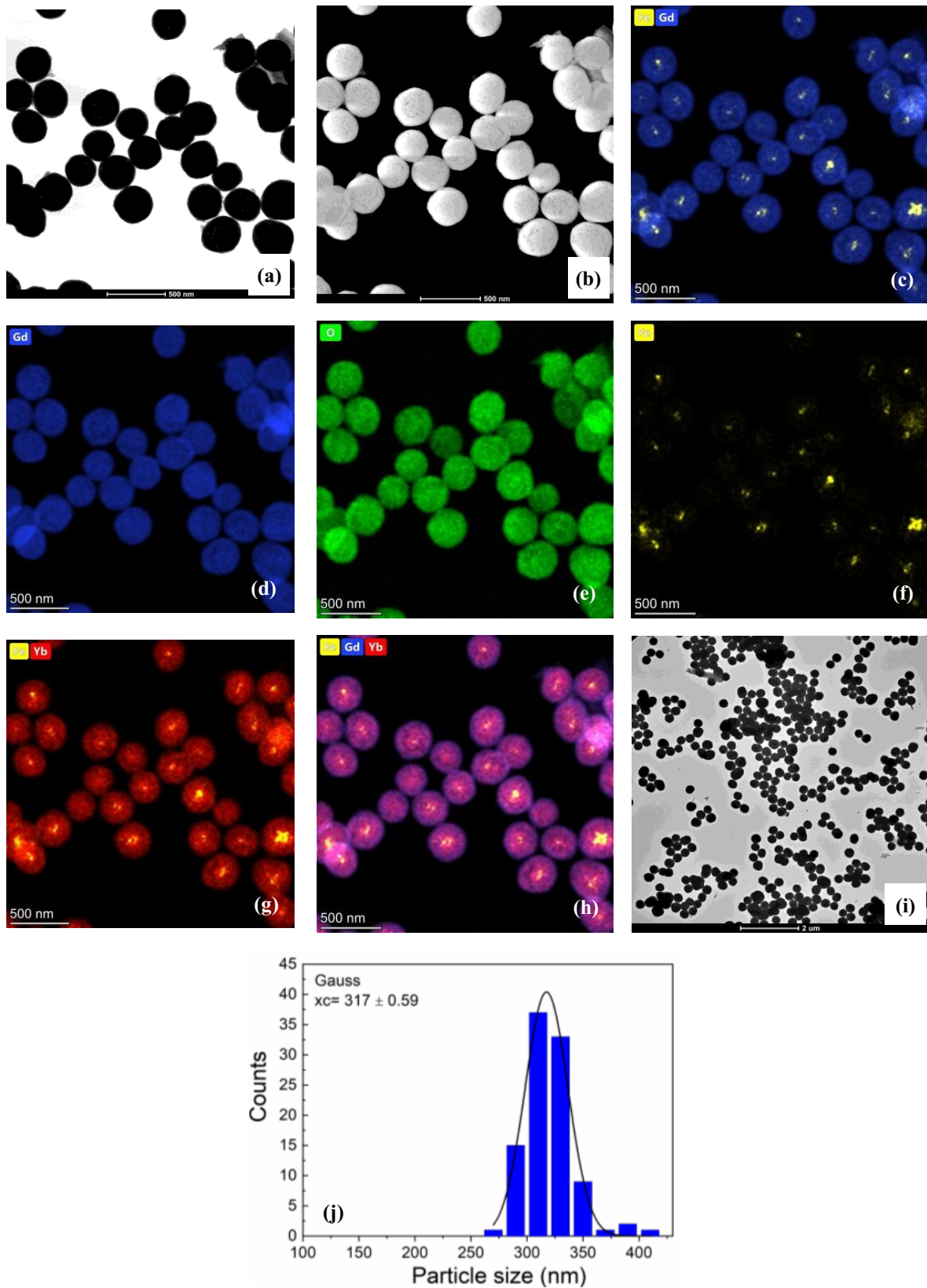


Fig. S5. TEM images of Fe₃O₄/Gd₂O₃:1% Er³⁺, 18% Yb³⁺, 2.5% Mg²⁺, 1% Nd³⁺ NPs in bright (a) and dark field (b). The distribution maps of the above-mentioned elements of the NPs Fe and Gd (c), Gd (d), O (e), Fe (f), Fe and Yb (g), Fe, Gd, and Yb (h), TEM image of the NPs (i). Histogram of NP size distribution (j).

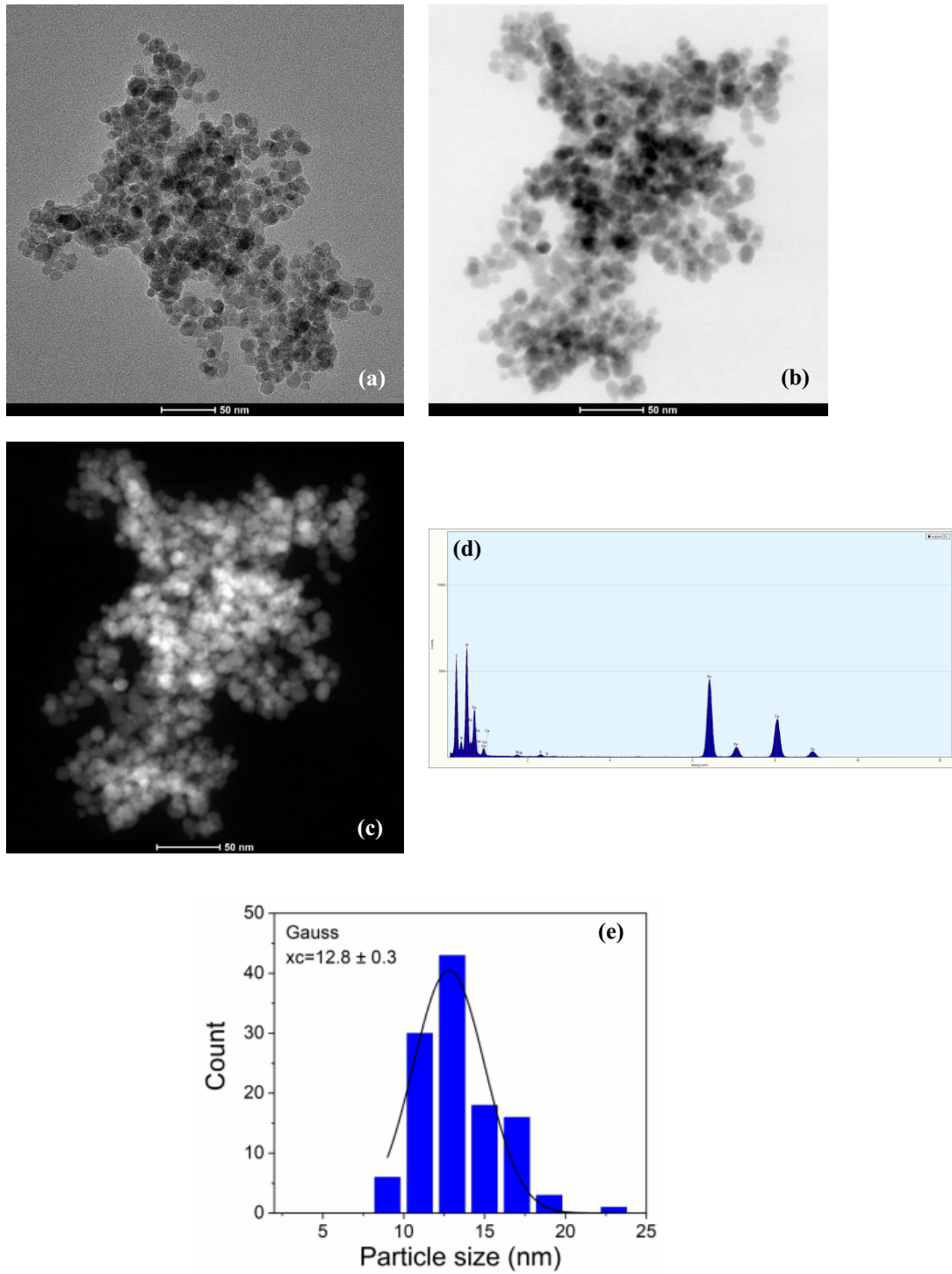


Fig. S6. TEM images of Fe₃O₄ NPs (a)–(c), EDX spectra of the NPs (d). Size distribution histograms of the NPs (e).

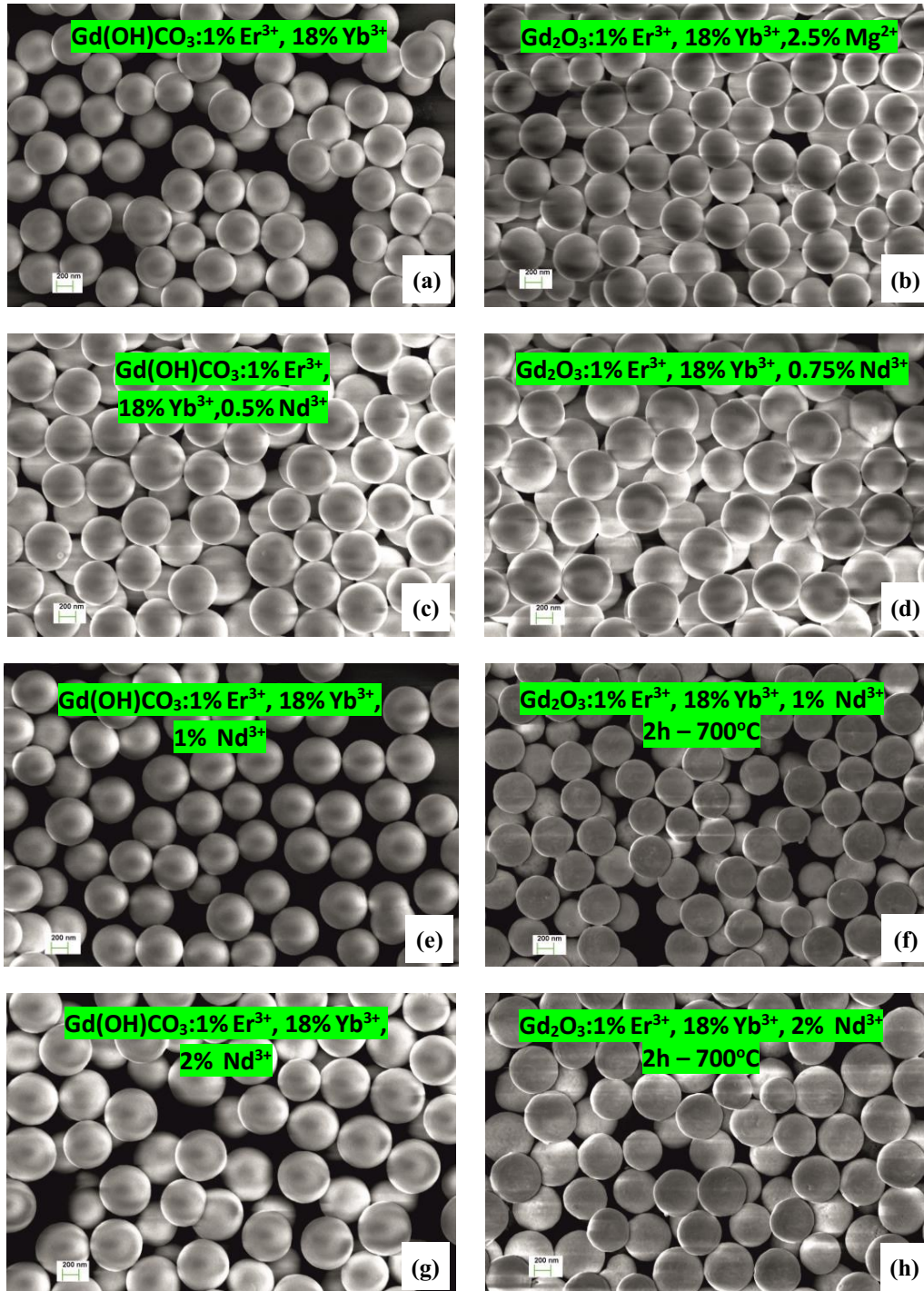


Fig. S7. SEM images of the $\text{Gd(OH)CO}_3:1\% \text{Er}^{3+}, 18\% \text{Yb}^{3+}$ (a), $\text{Gd}_2\text{O}_3:1\% \text{Er}^{3+}, 18\% \text{Yb}^{3+}, 2.5\% \text{Mg}^{2+}$ (b), $\text{Gd(OH)CO}_3:1\% \text{Er}^{3+}, 18\% \text{Yb}^{3+}, 0.5\% \text{Nd}^{3+}$ (c), $\text{Gd}_2\text{O}_3:1\% \text{Er}^{3+}, 18\% \text{Yb}^{3+}, 0.75\% \text{Nd}^{3+}$ (d), $\text{Gd(OH)CO}_3:1\% \text{Er}^{3+}, 18\% \text{Yb}^{3+}, 1\% \text{Nd}^{3+}$ (e), $\text{Gd}_2\text{O}_3:1\% \text{Er}^{3+}, 18\% \text{Yb}^{3+}, 1\% \text{Nd}^{3+}$ (calcined NPs at 700°C for 2 h) (f), $\text{Gd(OH)CO}_3:1\% \text{Er}^{3+}, 18\% \text{Yb}^{3+}, 2\% \text{Nd}^{3+}$ (g), and $\text{Gd}_2\text{O}_3:1\% \text{Er}^{3+}, 18\% \text{Yb}^{3+}, 2\% \text{Nd}^{3+}$ (calcined NPs at 700°C for 2 h) (h).

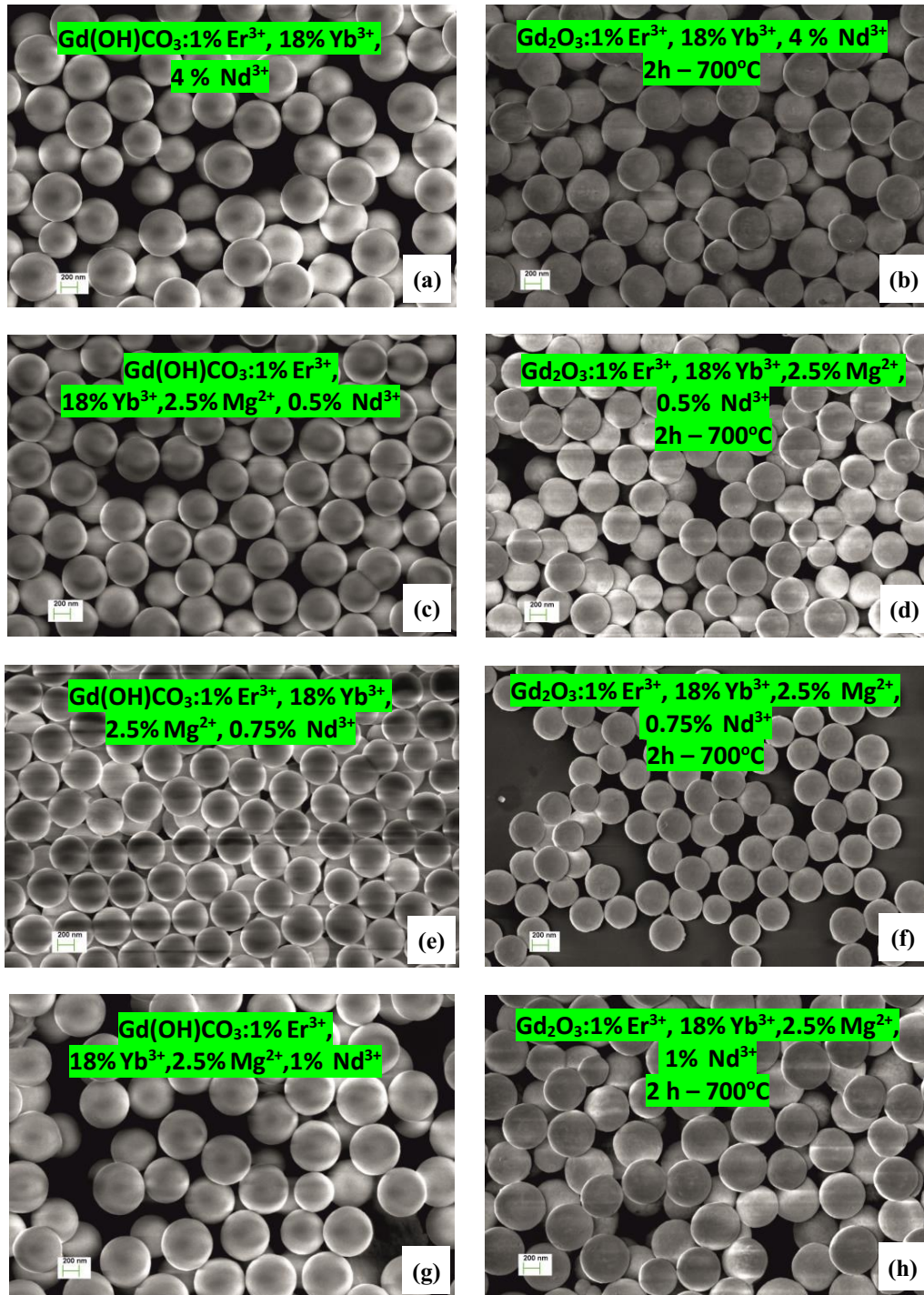


Fig. S8. SEM images of the $\text{Gd(OH)CO}_3:1\% \text{Er}^{3+}, 18\% \text{Yb}^{3+}, 4\% \text{Nd}^{3+}$ (a), $\text{Gd}_2\text{O}_3:1\% \text{Er}^{3+}, 18\% \text{Yb}^{3+}, 4\% \text{Nd}^{3+}$ (calcined NPs at 700°C for 2 h) (b), $\text{Gd(OH)CO}_3:1\% \text{Er}^{3+}, 18\% \text{Yb}^{3+}, 2.5\% \text{Mg}^{2+}, 0.5\% \text{Nd}^{3+}$ (c), $\text{Gd}_2\text{O}_3:1\% \text{Er}^{3+}, 18\% \text{Yb}^{3+}, 2.5\% \text{Mg}^{2+}, 0.5\% \text{Nd}^{3+}$ (calcined NPs at 700 °C for 2 h) (d), $\text{Gd(OH)CO}_3:1\% \text{Er}^{3+}, 18\% \text{Yb}^{3+}, 2.5\% \text{Mg}^{2+}, 0.75\% \text{Nd}^{3+}$ (e), $\text{Gd}_2\text{O}_3:1\% \text{Er}^{3+}, 18\% \text{Yb}^{3+}, 2.5\% \text{Mg}^{2+}, 0.75\% \text{Nd}^{3+}$ (calcined NPs at 700°C for 2 h) (f), $\text{Gd(OH)CO}_3:1\% \text{Er}^{3+}, 18\% \text{Yb}^{3+}, 2.5\% \text{Mg}^{2+}, 1\% \text{Nd}^{3+}$ (g), $\text{Gd}_2\text{O}_3:1\% \text{Er}^{3+}, 18\% \text{Yb}^{3+}, 2.5\% \text{Mg}^{2+}, 1\% \text{Nd}^{3+}$ (calcined NPs at 700 °C for 2 h) (h).

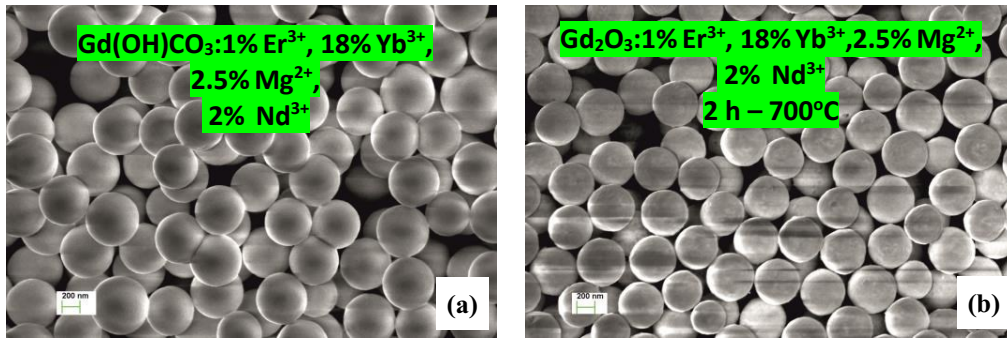


Fig. S9. SEM images of Gd(OH)CO₃:1% Er³⁺, 18% Yb³⁺, 2.5% Mg²⁺, 2% Nd³⁺ (a) and calcined NPs at 700° C for 2 h: Gd₂O₃:1% Er³⁺, 18% Yb³⁺, 2.5% Mg²⁺, 2% Nd³⁺ (b).

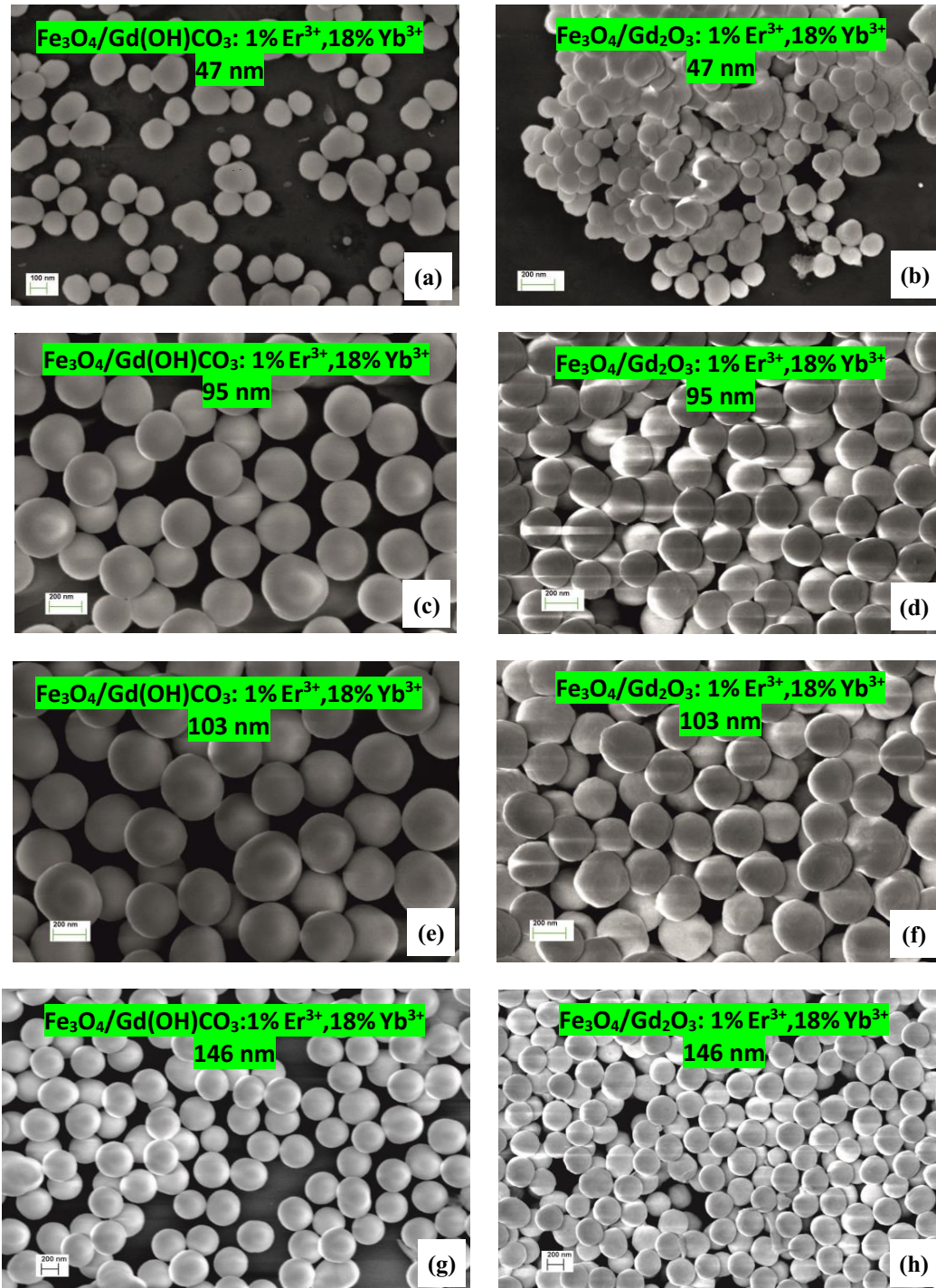


Fig. S10. SEM images of the $\text{Fe}_3\text{O}_4/\text{Gd}(\text{OH})\text{CO}_3:1\% \text{Er}^{3+}, 18\% \text{Yb}^{3+}$ (47 nm) (a), $\text{Fe}_3\text{O}_4/\text{Gd}_2\text{O}_3:1\% \text{Er}^{3+}, 18\% \text{Yb}^{3+}$ (calcined NPs at 700 °C for 2 h) (47 nm) (b), $\text{Fe}_3\text{O}_4/\text{Gd}(\text{OH})\text{CO}_3:1\% \text{Er}^{3+}, 18\% \text{Yb}^{3+}$ (95 nm) (c), $\text{Fe}_3\text{O}_4/\text{Gd}_2\text{O}_3:1\% \text{Er}^{3+}, 18\% \text{Yb}^{3+}$ (calcined NPs at 700 °C for 2 h) (95 nm) (d), $\text{Fe}_3\text{O}_4/\text{Gd}(\text{OH})\text{CO}_3:1\% \text{Er}^{3+}, 18\% \text{Yb}^{3+}$ (103 nm) (e), $\text{Fe}_3\text{O}_4/\text{Gd}_2\text{O}_3:1\% \text{Er}^{3+}, 18\% \text{Yb}^{3+}$ (calcined NPs at 700 °C for 2 h) (103 nm) (f), $\text{Fe}_3\text{O}_4/\text{Gd}(\text{OH})\text{CO}_3:1\% \text{Er}^{3+}, 18\% \text{Yb}^{3+}$ (146 nm) (g), $\text{Fe}_3\text{O}_4/\text{Gd}_2\text{O}_3:1\% \text{Er}^{3+}, 18\% \text{Yb}^{3+}$ (146 nm) (calcined NPs at 700 C for 2 h) NPs (h).

Table S2.
List of diameters of NPs obtained by homogeneous precipitation method.

	Sample composition	Particle size by SEM [nm]
1	Gd(OH)CO ₃ :1% Er ³⁺ , 18% Yb ³⁺	525.7 ± 1.84
2	Gd ₂ O ₃ :1% Er ³⁺ , 18% Yb ³⁺ , 2.5% Mg ²⁺	536 ± 6.11
3	Gd(OH)CO ₃ :1% Er ³⁺ , 18% Yb ³⁺ , 0.5% Nd ³⁺	582 ± 2.6
4	Gd ₂ O ₃ :1% Er ³⁺ , 18% Yb ³⁺ , 0.75% Nd ³⁺	615.5 ± 1.78
5	Gd(OH)CO ₃ :1% Er ³⁺ , 18% Yb ³⁺ , 1% Nd ³⁺	563.4 ± 3.4
6	Gd ₂ O ₃ :1% Er ³⁺ , 18% Yb ³⁺ , 1% Nd ³⁺	491.3 ± 2.7
7	Gd(OH)CO ₃ :1% Er ³⁺ , 18% Yb ³⁺ , 2% Nd ³⁺	622.4 ± 3.2
8	Gd ₂ O ₃ :1% Er ³⁺ , 18% Yb ³⁺ , 2% Nd ³⁺	572.8 ± 3.2
9	Gd(OH)CO ₃ :1% Er ³⁺ , 18% Yb ³⁺ , 4% Nd ³⁺	589.3 ± 3.4
10	Gd ₂ O ₃ :1% Er ³⁺ , 18% Yb ³⁺ , 4% Nd ³⁺	537.7 ± 1.14
11	Gd(OH)CO ₃ :1% Er ³⁺ , 18% Yb ³⁺ , 2.5% Mg ²⁺ , 0.5% Nd ³⁺	527.6 ± 1.3
12	Gd ₂ O ₃ :1% Er ³⁺ , 18% Yb ³⁺ , 2.5% Mg ²⁺ , 0.5% Nd ³⁺	475.3 ± 12.3
13	Gd(OH)CO ₃ :1% Er ³⁺ , 18% Yb ³⁺ , 2.5% Mg ²⁺ , 0.75% Nd ³⁺	474.6 ± 3.5
14	Gd ₂ O ₃ :1% Er ³⁺ , 18% Yb ³⁺ , 2.5% Mg ²⁺ , 0.75% Nd ³⁺	421.9 ± 2
15	Gd(OH)CO ₃ :1% Er ³⁺ , 18% Yb ³⁺ , 2.5% Mg ²⁺ , 1% Nd ³⁺	612.63 ± 4
16	Gd ₂ O ₃ :1% Er ³⁺ , 18% Yb ³⁺ , 2.5% Mg ²⁺ , 1% Nd ³⁺	551.5 ± 5
17	Gd(OH)CO ₃ :1% Er ³⁺ , 18% Yb ³⁺ , 2.5% Mg ²⁺ , 2% Nd ³⁺	564 ± 2
18	Gd ₂ O ₃ :1% Er ³⁺ , 18% Yb ³⁺ , 2.5% Mg ²⁺ , 2% Nd ³⁺	503.6 ± 3.41

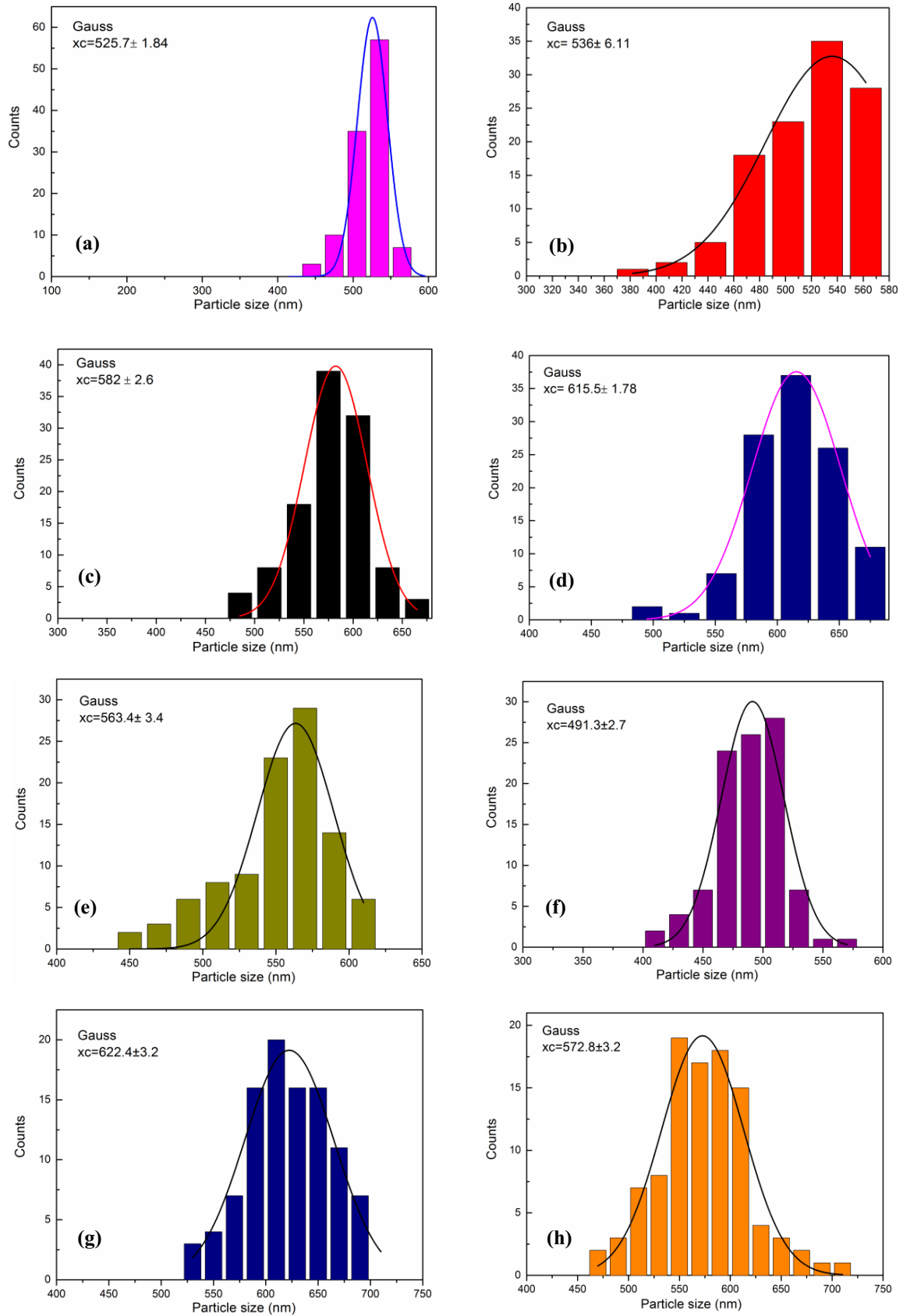


Fig. S11. Size distribution histograms of the $\text{Gd(OH)CO}_3:1\% \text{Er}^{3+}, 18\% \text{Yb}^{3+}$ (a), $\text{Gd}_2\text{O}_3:1\% \text{Er}^{3+}, 18\% \text{Yb}^{3+}, 2.5\% \text{Mg}^{2+}$ (b), $\text{Gd(OH)CO}_3:1\% \text{Er}^{3+}, 18\% \text{Yb}^{3+}, 0.5\% \text{Nd}^{3+}$ (c), $\text{Gd}_2\text{O}_3:1\% \text{Er}^{3+}, 18\% \text{Yb}^{3+}, 0.75\% \text{Nd}^{3+}$ (d), $\text{Gd(OH)CO}_3:1\% \text{Er}^{3+}, 18\% \text{Yb}^{3+}, 1\% \text{Nd}^{3+}$ (e), $\text{Gd}_2\text{O}_3:1\% \text{Er}^{3+}, 18\% \text{Yb}^{3+}, 1\% \text{Nd}^{3+}$ (f), $\text{Gd(OH)CO}_3:1\% \text{Er}^{3+}, 18\% \text{Yb}^{3+}, 2\% \text{Nd}^{3+}$ (g), $\text{Gd}_2\text{O}_3:1\% \text{Er}^{3+}, 18\% \text{Yb}^{3+}, 2\% \text{Nd}^{3+}$ NPs (h).

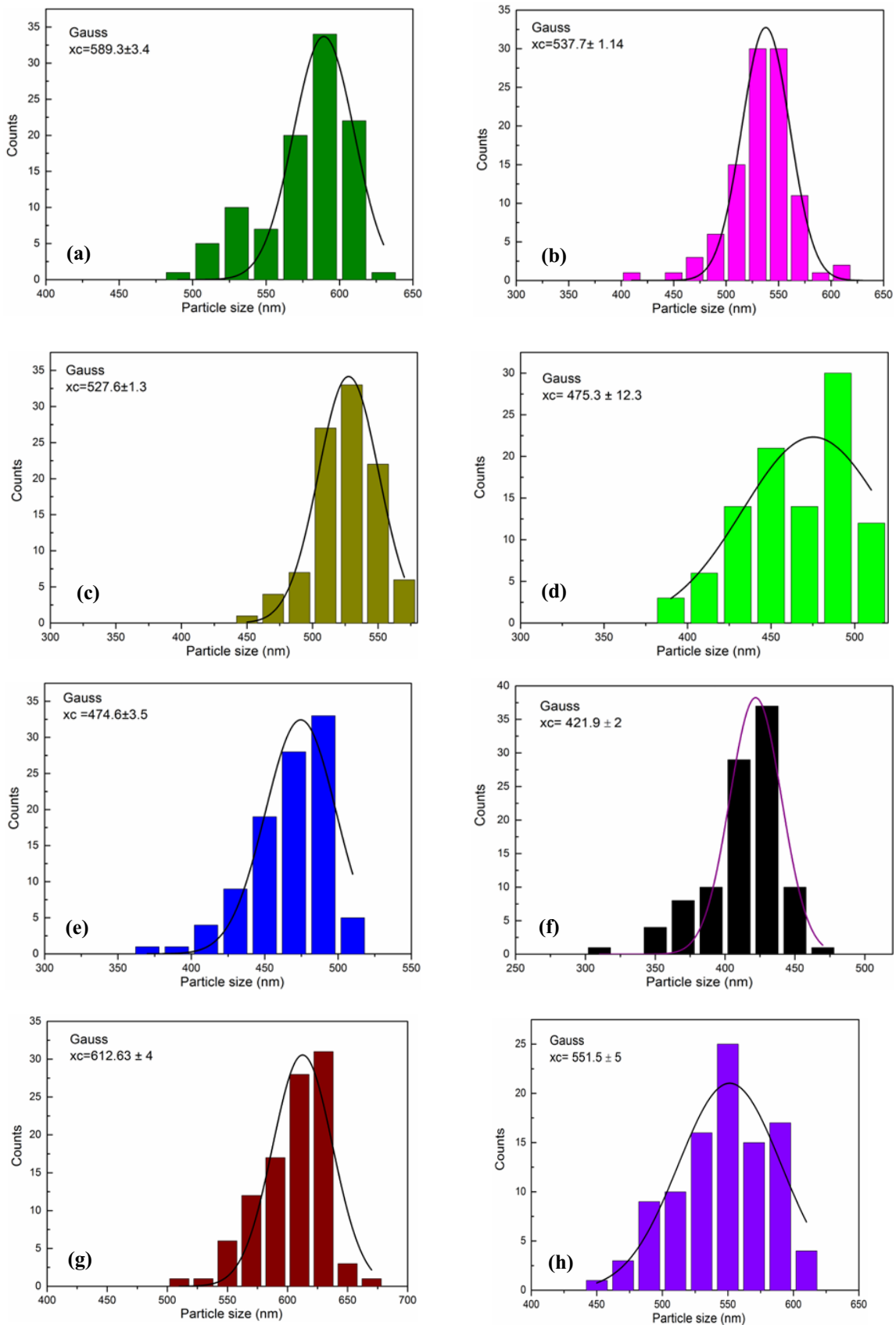


Fig. S12. Size distribution histograms of the $\text{Gd}(\text{OH})\text{CO}_3:1\% \text{Er}^{3+}, 18\% \text{Yb}^{3+}, 4\% \text{Nd}^{3+}$ (a) $\text{Gd}_2\text{O}_3:1\% \text{Er}^{3+}, 18\% \text{Yb}^{3+}, 4\% \text{Nd}^{3+}$ (b) $\text{Gd}(\text{OH})\text{CO}_3:1\% \text{Er}^{3+}, 18\% \text{Yb}^{3+}, 2.5\% \text{Mg}^{2+}, 0.5\% \text{Nd}^{3+}$ (c) $\text{Gd}_2\text{O}_3:1\% \text{Er}^{3+}, 18\% \text{Yb}^{3+}, 2.5\% \text{Mg}^{2+}, 0.5\% \text{Nd}^{3+}$ (d) $\text{Gd}(\text{OH})\text{CO}_3:1\% \text{Er}^{3+}, 18\% \text{Yb}^{3+}, 2.5\% \text{Mg}^{2+}, 0.75\% \text{Nd}^{3+}$ (e) $\text{Gd}_2\text{O}_3:1\% \text{Er}^{3+}, 18\% \text{Yb}^{3+}, 2.5\% \text{Mg}^{2+}, 0.75\% \text{Nd}^{3+}$ (f) $\text{Gd}(\text{OH})\text{CO}_3:1\% \text{Er}^{3+}, 18\% \text{Yb}^{3+}, 2.5\% \text{Mg}^{2+}, 1\% \text{Nd}^{3+}$ (g) $\text{Gd}_2\text{O}_3:1\% \text{Er}^{3+}, 18\% \text{Yb}^{3+}, 2.5\% \text{Mg}^{2+}, 1\% \text{Nd}^{3+}$ NPs (h).

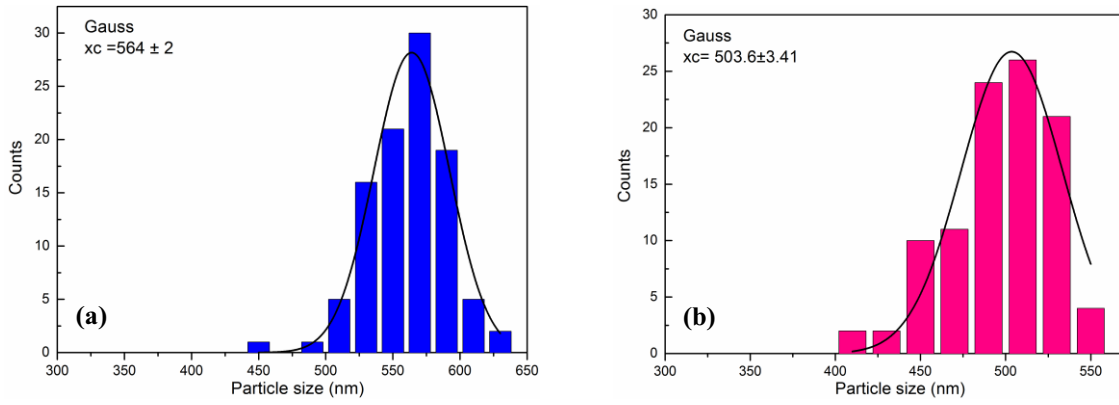


Fig. S13. Size distribution histograms of the $\text{Gd(OH)CO}_3:1\% \text{Er}^{3+}$, $18\% \text{Yb}^{3+}$, $2.5\% \text{Mg}^{2+}$, $2\% \text{Nd}^{3+}$ (a), $\text{Gd}_2\text{O}_3:1\% \text{Er}^{3+}$, $18\% \text{Yb}^{3+}$, $2.5\% \text{Mg}^{2+}$, $2\% \text{Nd}^{3+}$ NPs (b).

Table S3.

The number of photons involved in the anti-Stokes emission process for $\text{Fe}_3\text{O}_4/\text{Gd}_2\text{O}_3:1\% \text{Er}^{3+}$, $18\% \text{Yb}^{3+}$ NPs (powder form).

Thicknesses of Gd_2O_3 shells [nm]	Composition	Green luminescence	Red luminescence
		(560 nm) $^4\text{S}_{3/2} \rightarrow ^4\text{I}_{15/2}$, $^2\text{H}_{11/2} \rightarrow ^4\text{I}_{15/2}$	(662 nm) $^4\text{F}_{9/2} \rightarrow ^4\text{I}_{15/2}$
47 nm	$\text{Fe}_3\text{O}_4/\text{Gd}_2\text{O}_3:1\% \text{Er}^{3+}$, $18\% \text{Yb}^{3+}$	—	1.47 ± 0.03
95 nm		1.89 ± 0.05	1.53 ± 0.02
103 nm		1.80 ± 0.06	1.39 ± 0.03
146 nm		1.82 ± 0.08	1.53 ± 0.03

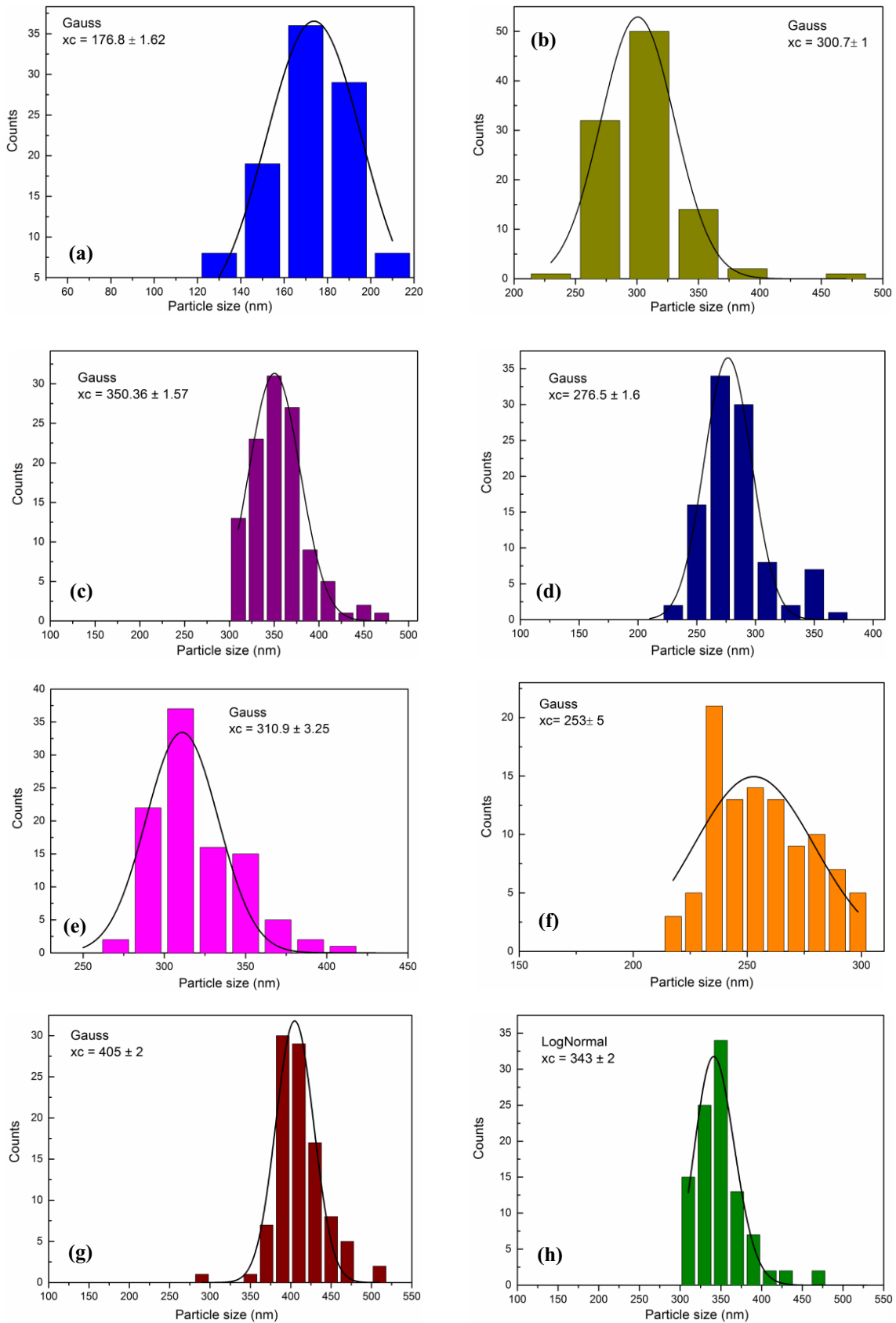


Fig. S14. Size distribution histograms of the $\text{Fe}_3\text{O}_4/\text{Gd}(\text{OH})\text{CO}_3:1\% \text{Er}^{3+}, 18\% \text{Yb}^{3+}$ (47 nm) (a), $\text{Fe}_3\text{O}_4/\text{Gd}_2\text{O}_3:1\% \text{Er}^{3+}, 18\% \text{Yb}^{3+}$ (calcined NPs at 700°C for 2 h) (47 nm) (b), $\text{Fe}_3\text{O}_4/\text{Gd}(\text{OH})\text{CO}_3:1\% \text{Er}^{3+}, 18\% \text{Yb}^{3+}$ (103 nm) (c), $\text{Fe}_3\text{O}_4/\text{Gd}_2\text{O}_3:1\% \text{Er}^{3+}, 18\% \text{Yb}^{3+}$ (calcined NPs at 700°C for 2 h) (103 nm) (d), $\text{Fe}_3\text{O}_4/\text{Gd}(\text{OH})\text{CO}_3:1\% \text{Er}^{3+}, 18\% \text{Yb}^{3+}$ (95 nm) (e), $\text{Fe}_3\text{O}_4/\text{Gd}_2\text{O}_3:1\% \text{Er}^{3+}, 18\% \text{Yb}^{3+}$ (calcined NPs at 700°C for 2 h) (95 nm) (f), $\text{Fe}_3\text{O}_4/\text{Gd}(\text{OH})\text{CO}_3:1\% \text{Er}^{3+}, 18\% \text{Yb}^{3+}$ (146 nm) (g), $\text{Fe}_3\text{O}_4/\text{Gd}_2\text{O}_3:1\% \text{Er}^{3+}, 18\% \text{Yb}^{3+}$ (calcined NPs at 700°C for 2 h) (146 nm) NPs (h).

Table S4

List of diameters of NPs obtained by the homogeneous precipitation method.

	Sample composition	Particle size by SEM [nm]
1	Fe ₃ O ₄ /Gd(OH)CO ₃ :1% Er ³⁺ , 18% Yb ³⁺ (47 nm)	176.8 ± 1.62
2	Fe ₃ O ₄ /Gd ₂ O ₃ :1% Er ³⁺ , 18% Yb ³⁺ (47 nm)	300.7 ± 1
3	Fe ₃ O ₄ /Gd(OH)CO ₃ :1% Er ³⁺ , 18% Yb ³⁺ (103 nm)	350.36 ± 1.57
4	Fe ₃ O ₄ /Gd ₂ O ₃ :1% Er ³⁺ , 18% Yb ³⁺ (103 nm)	276.5 ± 1.6
5	Fe ₃ O ₄ /Gd(OH)CO ₃ :1% Er ³⁺ , 18% Yb ³⁺ (95 nm)	310.9 ± 3.25
6	Fe ₃ O ₄ /Gd ₂ O ₃ :1% Er ³⁺ , 18% Yb ³⁺ (95 nm)	253 ± 5
7	Fe ₃ O ₄ /Gd(OH)CO ₃ :1% Er ³⁺ , 18% Yb ³⁺ (146 nm)	405 ± 2
8	Fe ₃ O ₄ /Gd ₂ O ₃ :1% Er ³⁺ , 18% Yb ³⁺ (146 nm)	343 ± 2

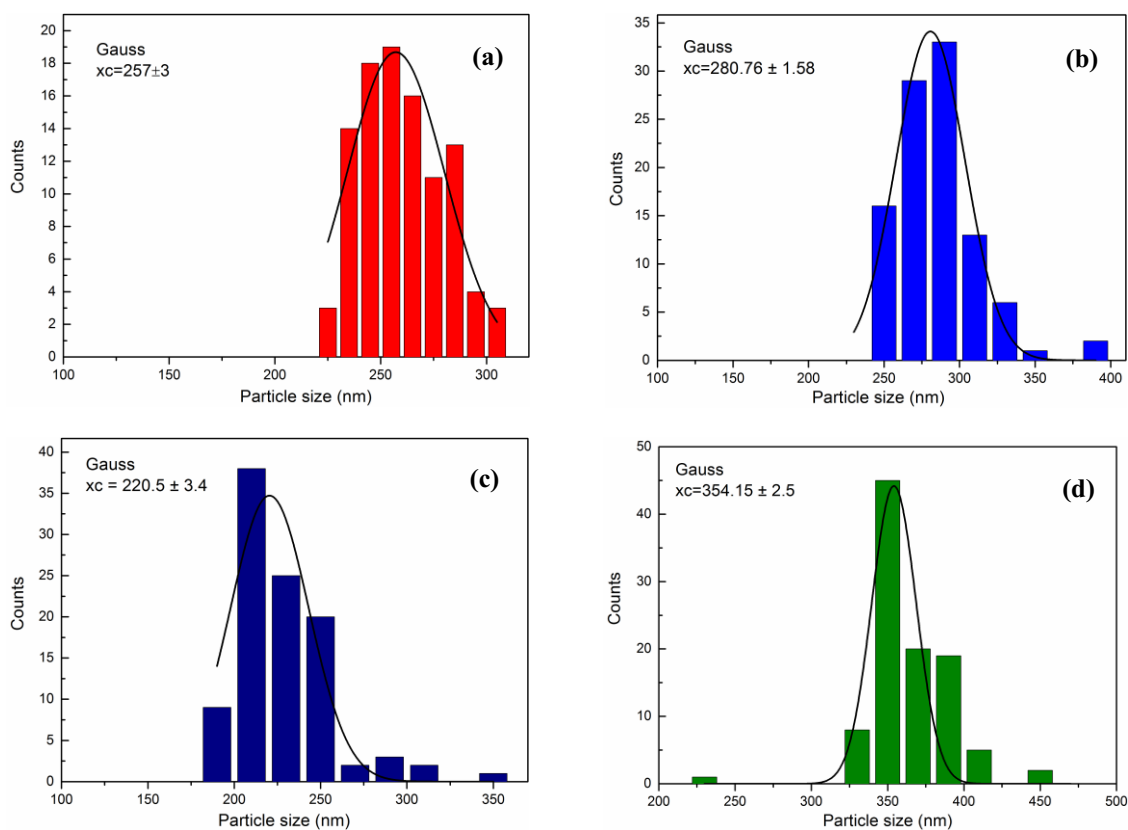


Fig. S15. Size distribution histograms of the Fe₃O₄/Gd(OH)CO₃:1% Er³⁺, 18% Yb³⁺, 2.5% Mg²⁺, 0.5% Nd³⁺ (a), Fe₃O₄/Gd(OH)CO₃:1% Er³⁺, 18% Yb³⁺, 2.5% Mg²⁺, 0.75% Nd³⁺ (b), Fe₃O₄/Gd₂O₃:1% Er³⁺, 18% Yb³⁺, 2.5% Mg²⁺, 0.75% Nd³⁺ (calined at 700 °C for 2 h) (c), Fe₃O₄/Gd(OH)CO₃:1% Er³⁺, 18% Yb³⁺, 2.5% Mg²⁺, 1% Nd³⁺ NPs (d).

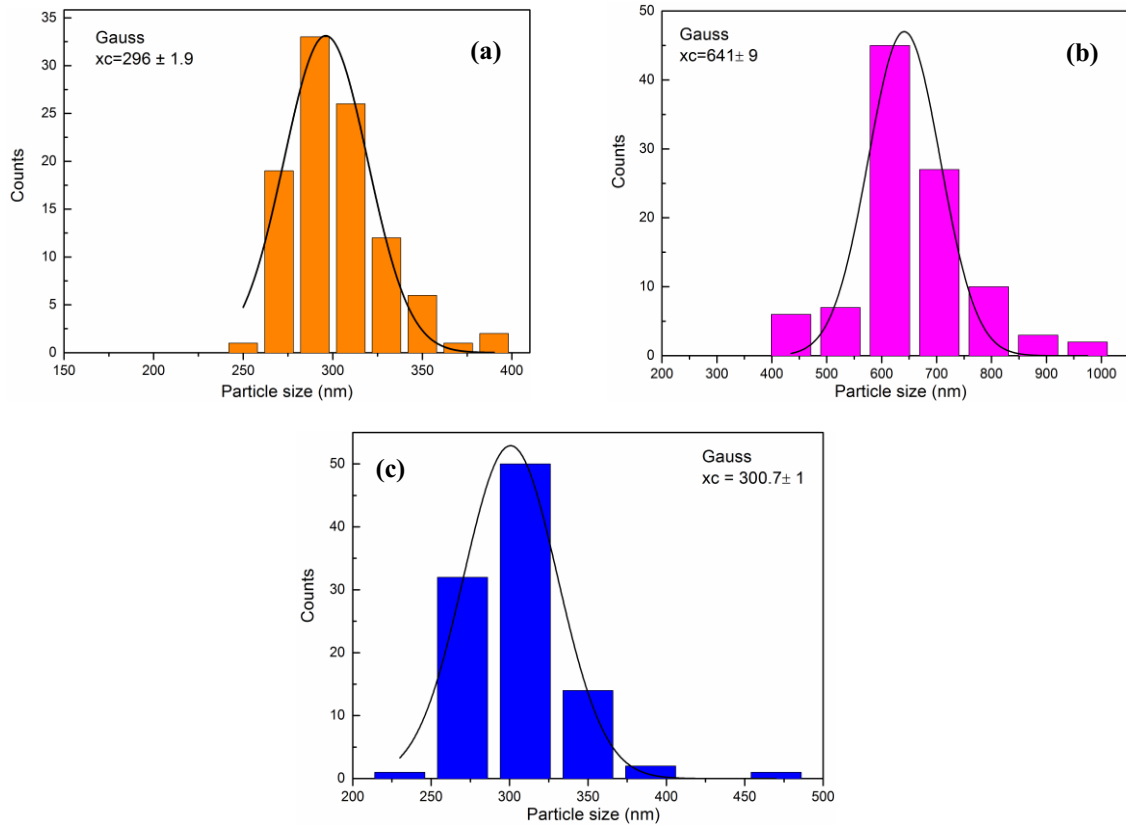


Fig. S16. Size distribution histograms of the $\text{Fe}_3\text{O}_4/\text{Gd}_2\text{O}_3:1\% \text{Er}^{3+}$, $18\% \text{Yb}^{3+}$, $2.5\% \text{Mg}^{2+}$, $1\% \text{Nd}^{3+}$ (calcined at 700°C for 2 h) (a), $\text{Fe}_3\text{O}_4/\text{Gd}_2\text{O}_3:1\% \text{Er}^{3+}$, $18\% \text{Yb}^{3+}$, $2.5\% \text{Mg}^{2+}$, $2\% \text{Nd}^{3+}$ (calcined at 700°C for 2 h) (b), $\text{Fe}_3\text{O}_4/\text{Gd}_2\text{O}_3:1\% \text{Er}^{3+}$, $18\% \text{Yb}^{3+}$, $2.5\% \text{Mg}^{2+}$, $4\% \text{Nd}^{3+}$ (calcined at 700°C for 2 h) (c).

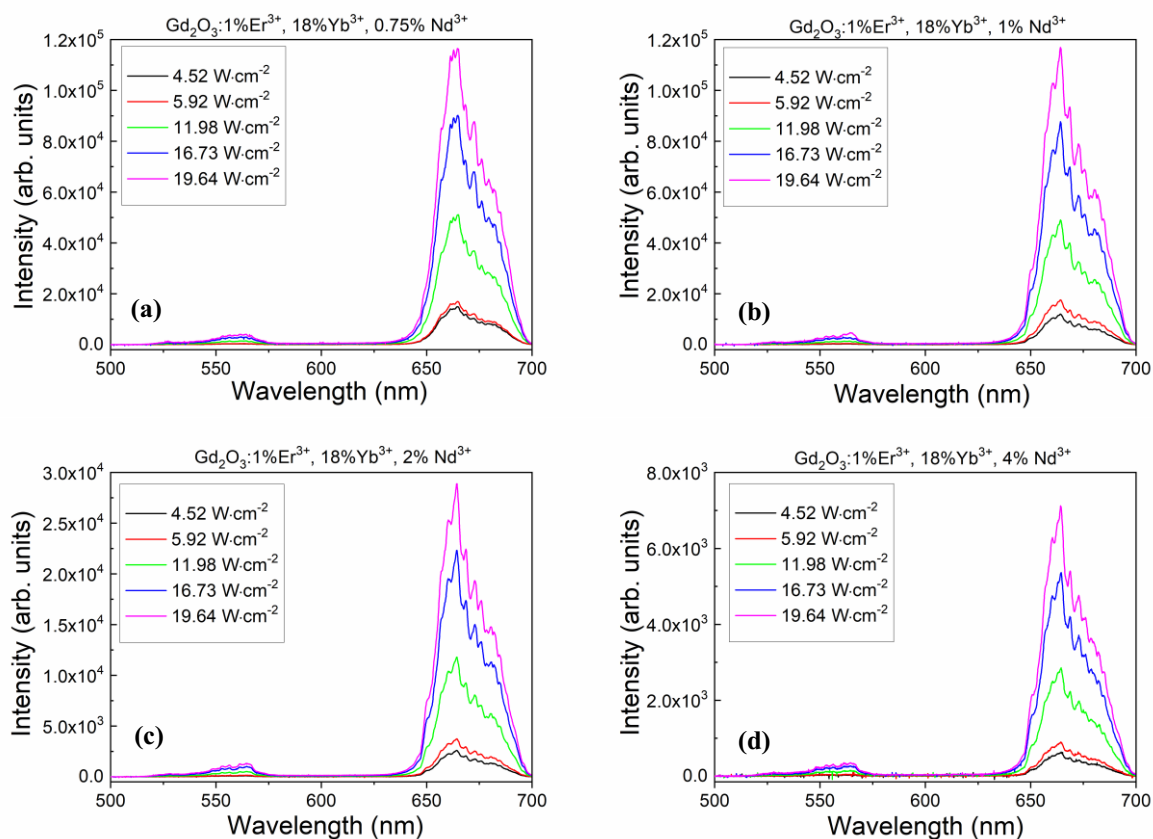


Fig. S17. PL spectra of the Gd₂O₃:1% Er³⁺, 18% Yb³⁺, 0.75% Nd³⁺ (a), Gd₂O₃:1% Er³⁺, 18% Yb³⁺, 1% Nd³⁺ (b), Gd₂O₃:1% Er³⁺, 18% Yb³⁺, 2% Nd³⁺ (c), Gd₂O₃:1% Er³⁺, 18% Yb³⁺, 4% Nd³⁺ NPs (in powder form) measured for five laser power densities of 980 nm (d).

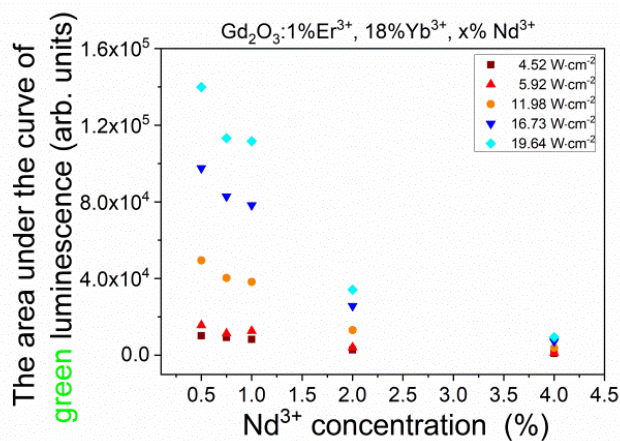


Fig. S18. Area under the curve of green luminescence as a function of neodymium ion concentration determined for five laser power densities of 980 nm for Gd₂O₃:1% Er³⁺, 18% Yb³⁺, x% Nd³⁺ NPs.

Table S5.
List of diameters of NPs obtained by the homogeneous precipitation method.

	Sample composition	Particle size by SEM (nm)
1	Fe ₃ O ₄ /Gd(OH)CO ₃ :1% Er ³⁺ , 18% Yb ³⁺ , 2.5% Mg ²⁺ , 0.5% Nd ³⁺	257 ± 3
2	Fe ₃ O ₄ /Gd(OH)CO ₃ :1% Er ³⁺ , 18% Yb ³⁺ , 2.5% Mg ²⁺ , 0.75% Nd ³⁺	280.76 ± 1.58
3	Fe ₃ O ₄ /Gd ₂ O ₃ :1% Er ³⁺ , 18% Yb ³⁺ , 2.5% Mg ²⁺ , 0.75% Nd ³⁺	220.5 ± 3.4
4	Fe ₃ O ₄ /Gd(OH)CO ₃ :1% Er ³⁺ , 18% Yb ³⁺ , 2.5% Mg ²⁺ , 1% Nd ³⁺	354.15 ± 2.5
5	Fe ₃ O ₄ /Gd ₂ O ₃ :1% Er ³⁺ , 18% Yb ³⁺ , 2.5% Mg ²⁺ , 1% Nd ³⁺	296 ± 1.9
6	Fe ₃ O ₄ /Gd ₂ O ₃ :1% Er ³⁺ , 18% Yb ³⁺ , 2.5% Mg ²⁺ , 2% Nd ³⁺	641 ± 9
7	Fe ₃ O ₄ /Gd ₂ O ₃ :1% Er ³⁺ , 18% Yb ³⁺ , 2.5% Mg ²⁺ , 4% Nd ³⁺	300.7 ± 1

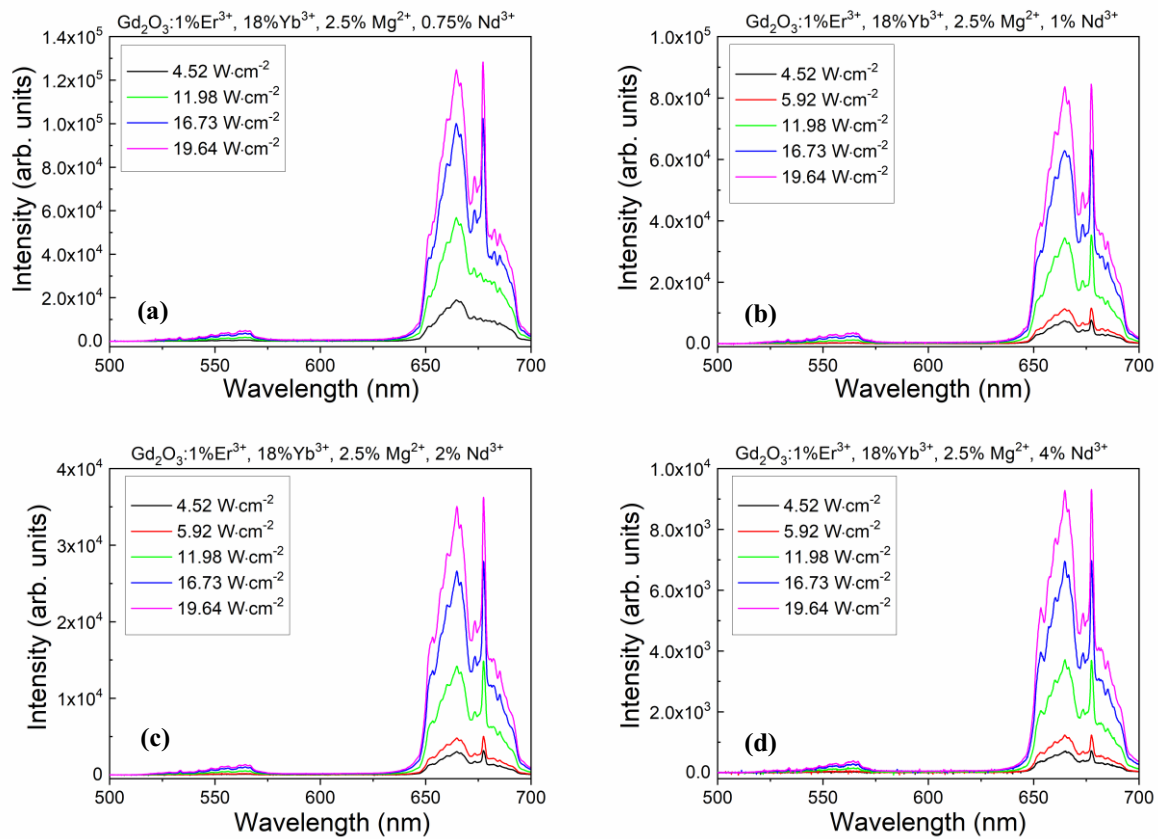


Fig. S19. PL spectra of the Gd₂O₃:1%Er³⁺, 18%Yb³⁺, 2.5%Mg²⁺, 0.75%Nd³⁺ (a), Gd₂O₃:1%Er³⁺, 18%Yb³⁺, 2.5%Mg²⁺, 1%Nd³⁺ (b), Gd₂O₃:1%Er³⁺, 18%Yb³⁺, 2.5%Mg²⁺, 2%Nd³⁺ (c), Gd₂O₃:1%Er³⁺, 18%Yb³⁺, 2.5%Mg²⁺, 4%Nd³⁺ NPs measured for five laser power densities of 980 nm (d).

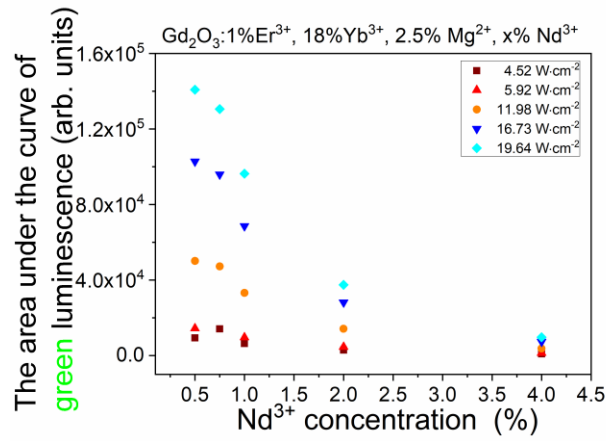


Fig. S20. Area under the curve of green luminescence as a function of neodymium ion concentration determined for five laser power densities of 980 nm for $\text{Gd}_2\text{O}_3:1\%\text{Er}^{3+}, 18\%\text{Yb}^{3+}, 2.5\%\text{Mg}^{2+}, x\%\text{Nd}^{3+}$ NPs.

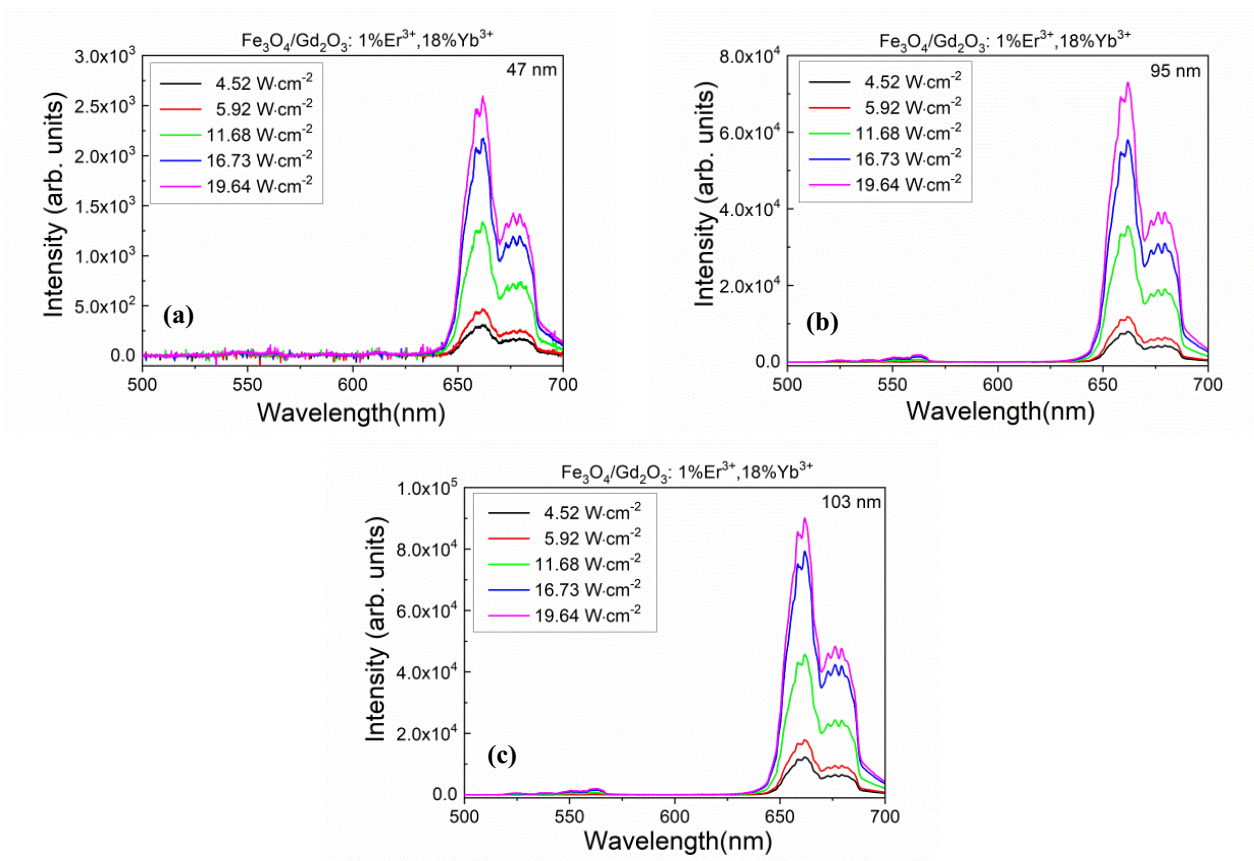


Fig. S21. PL spectra of the $\text{Fe}_3\text{O}_4/\text{Gd}_2\text{O}_3:1\%\text{Er}^{3+}, 18\%\text{Yb}^{3+}$ NPs measured for five laser power densities of 980 nm. The spectra obtained for different thicknesses of the shells $\text{Gd}_2\text{O}_3:1\%\text{Er}^{3+}, 18\%\text{Yb}^{3+}$ NPs 47 nm (a), 95 nm (b), 103 nm (c).

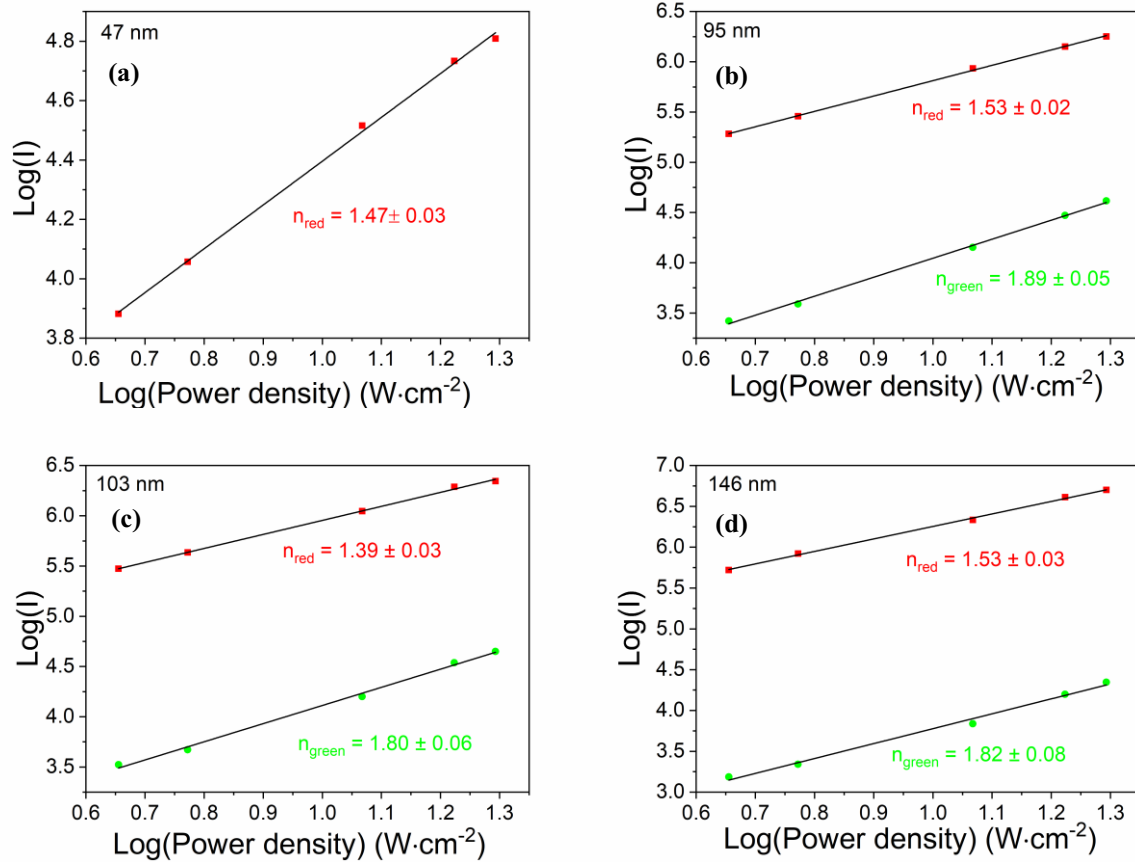


Fig. S22. Logarithmic dependence of the anti-Stokes emission intensity as a function of power density of a semiconductor laser with a wavelength of 980 nm (continuous wave) for $\text{Fe}_3\text{O}_4/\text{Gd}_2\text{O}_3:1\% \text{Er}^{3+}, 18\% \text{Yb}^{3+}$ NPs with different thicknesses of Gd_2O_3 shells. The NPs were in the form of powder.

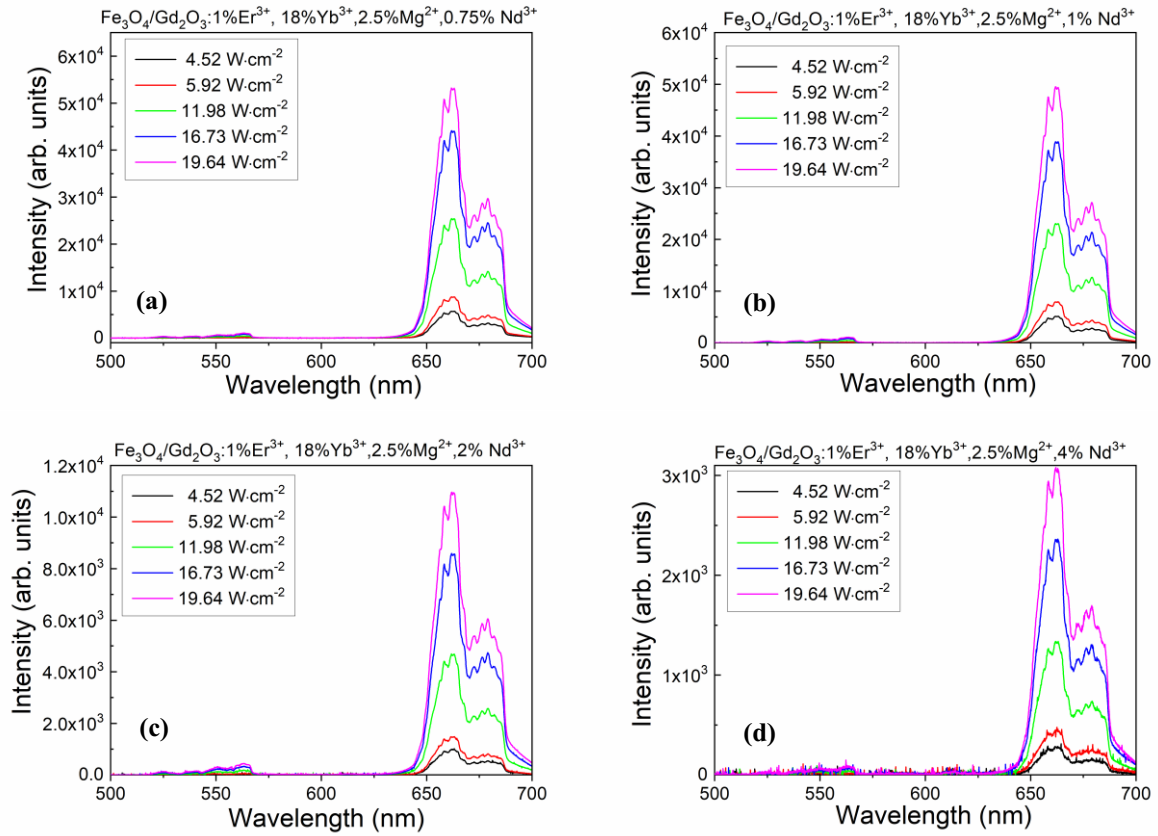


Fig. S23. PL spectra of the $\text{Fe}_3\text{O}_4/\text{Gd}_2\text{O}_3:1\%\text{Er}^{3+}, 18\%\text{Yb}^{3+}, 2.5\%\text{Mg}^{2+}, 0.75\%\text{Nd}^{3+}$ (a), $\text{Fe}_3\text{O}_4/\text{Gd}_2\text{O}_3:1\%\text{Er}^{3+}, 18\%\text{Yb}^{3+}, 2.5\%\text{Mg}^{2+}, 1\%\text{Nd}^{3+}$ (b), $\text{Fe}_3\text{O}_4/\text{Gd}_2\text{O}_3:1\%\text{Er}^{3+}, 18\%\text{Yb}^{3+}, 2.5\%\text{Mg}^{2+}, 2\%\text{Nd}^{3+}$ (c), $\text{Fe}_3\text{O}_4/\text{Gd}_2\text{O}_3:1\%\text{Er}^{3+}, 18\%\text{Yb}^{3+}, 2.5\%\text{Mg}^{2+}, 4\%\text{Nd}^{3+}$ NPs (d). The NPs (in powder form) were excited with five power densities of a semiconductor laser with a wavelength of 980 nm.

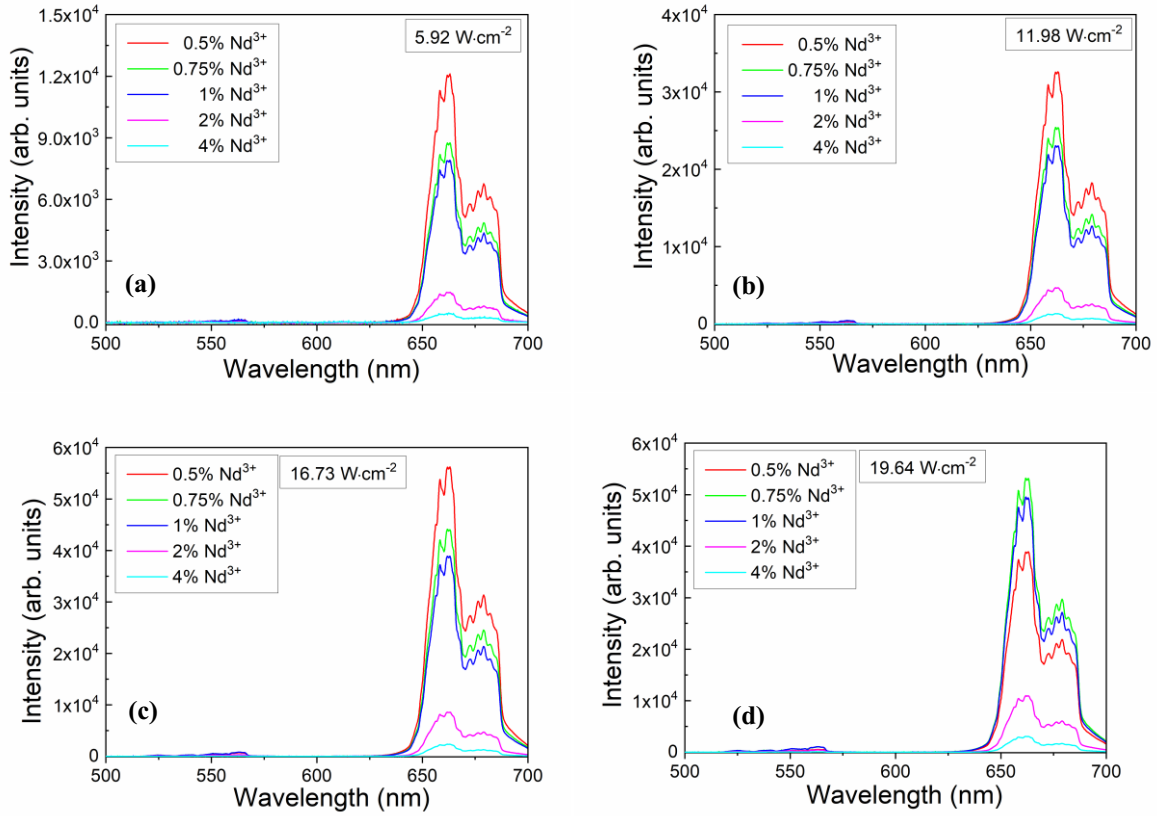


Fig. S24. PL spectra of the $\text{Fe}_3\text{O}_4/\text{Gd}_2\text{O}_3:1\% \text{Er}^{3+}, 18\% \text{Yb}^{3+}, 2.5\% \text{Mg}^{2+}, x\% \text{Nd}^{3+}$ NPs doped with different concentrations of neodymium ions, measured at four power densities of a 980 nm semiconductor laser $5.92 \text{ W}\cdot\text{cm}^{-2}$ (a), $11.98 \text{ W}\cdot\text{cm}^{-2}$ (b), $16.73 \text{ W}\cdot\text{cm}^{-2}$ (c), $19.64 \text{ W}\cdot\text{cm}^{-2}$ (d).

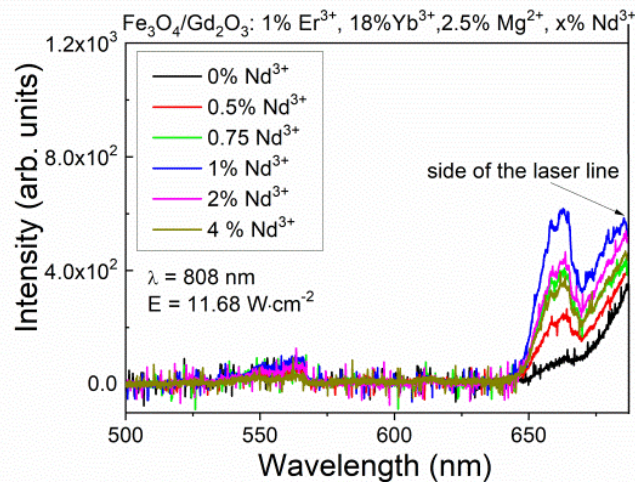


Fig. S25. PL spectra of the $\text{Fe}_3\text{O}_4/\text{Gd}_2\text{O}_3:1\% \text{Er}^{3+}, 18\% \text{Yb}^{3+}, 2.5\% \text{Mg}^{2+}, x\% \text{Nd}^{3+}$ NPs doped with different concentrations of Nd^{3+} ions, measured for laser with a wavelength of 808 nm. The laser power density was $11.68 \text{ W}\cdot\text{cm}^{-2}$.

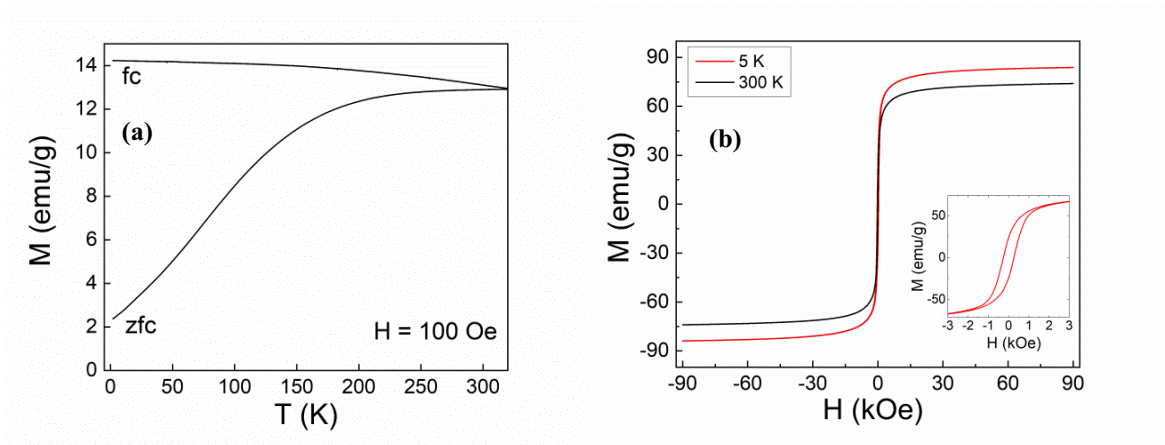


Fig. S26. ZFC/FC measurements at $H = 100$ Oe (a), and magnetization curves measured at 300 K and 5 K for Fe_3O_4 (b). The inset to (b) shows a low-field range of the hysteresis loop measured at 5 K.

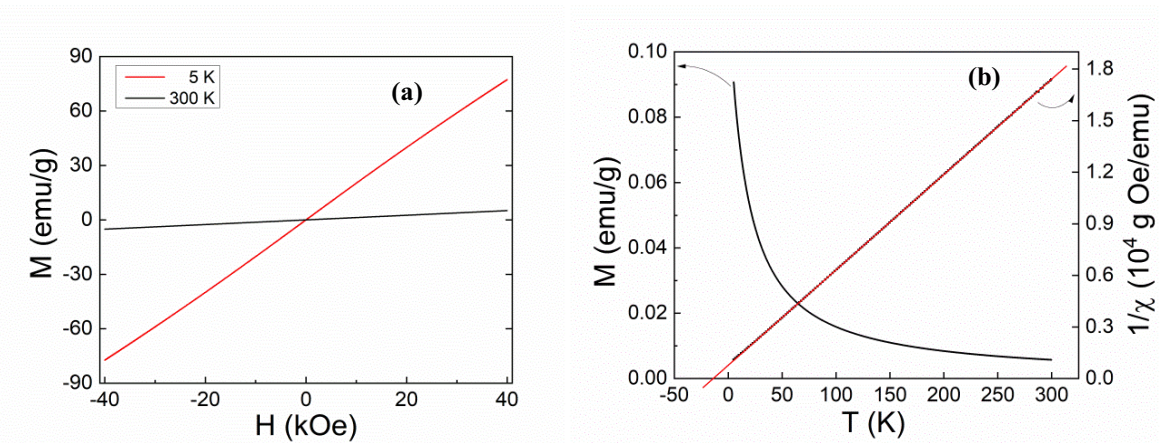


Fig. S27. Magnetization curves for $\text{Gd}_2\text{O}_3:1\% \text{Er}^{3+}$, $18\% \text{Yb}^{3+}$ measured at 300 K and 5 K (a). Temperature dependence of the magnetization and inverse susceptibility for $\text{Gd}_2\text{O}_3:1\% \text{Er}^{3+}$, $18\% \text{Yb}^{3+}$ NPs at $H = 100$ Oe (b). The red line is the result of the Curie-Weiss fitting.

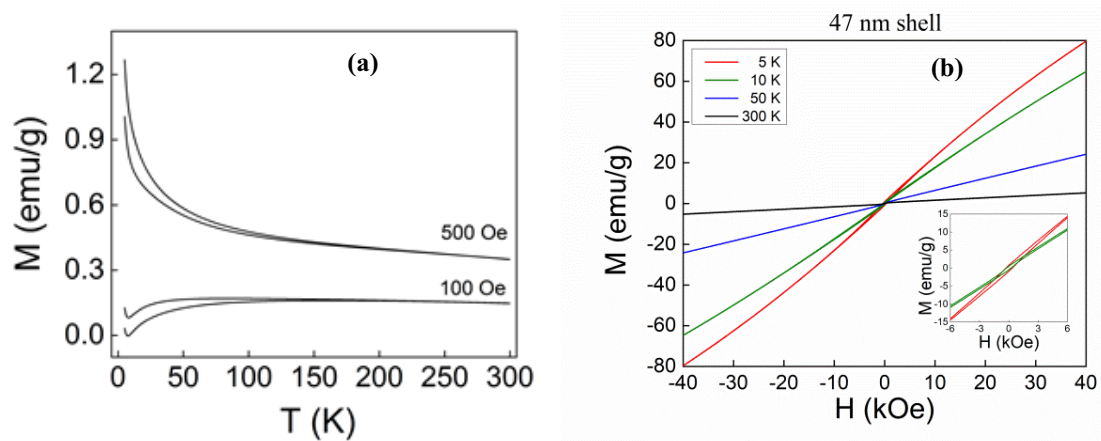


Fig. S28. ZFC-FC curves for $\text{Fe}_3\text{O}_4/\text{Gd}_2\text{O}_3:1\% \text{Er}^{3+}$, $18\% \text{Yb}^{3+}$ (shell thickness of 47 nm – black lines) measured at 100 Oe (a). Magnetization curves for $\text{Fe}_3\text{O}_4/\text{Gd}_2\text{O}_3:1\% \text{Er}^{3+}$, $18\% \text{Yb}^{3+}$ with a 47 nm shell measured at selected temperatures (b).

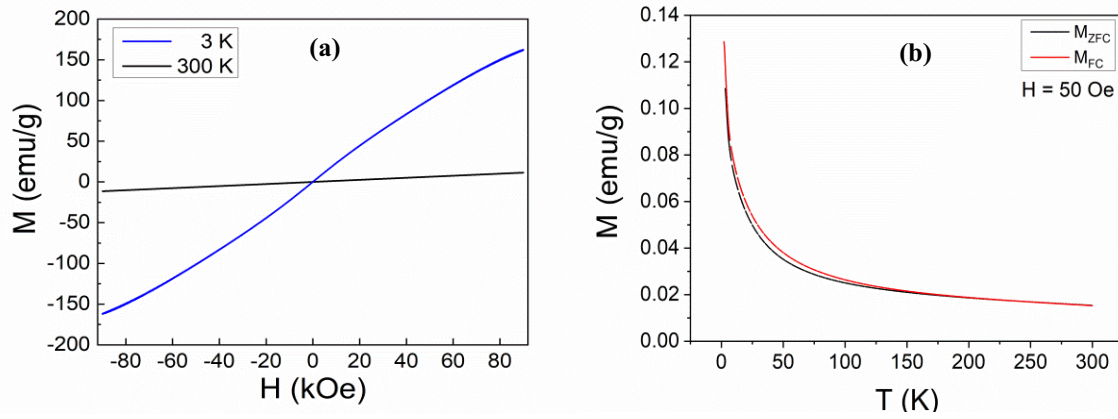


Fig. S29. Magnetization as a function of the magnetic field measured at 3 and 300 K (a), ZFC and FC curves for $\text{Fe}_3\text{O}_4/\text{Gd}_2\text{O}_3:1\% \text{Er}^{3+}, 18\% \text{Yb}^{3+}, 2.5\% \text{Mg}^{2+}, 0.5\% \text{Nd}^{3+}$ NPs (b).

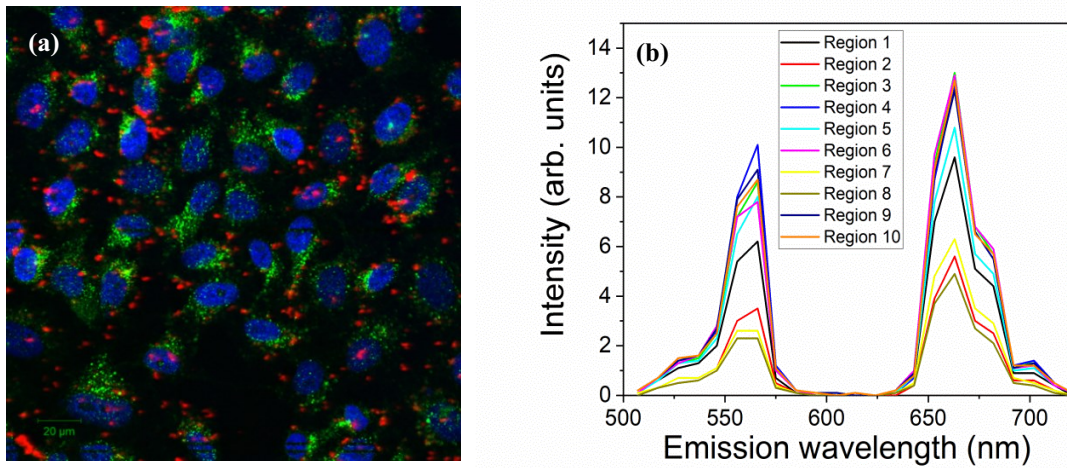


Fig. S30. (a) Confocal image of HeLa cancer cells after a 24 h incubation in a solution with $50 \mu\text{g}\cdot\text{ml}^{-1}$ of $\text{Fe}_3\text{O}_4/\text{Gd}_2\text{O}_3:1\% \text{Er}^{3+}, 18\% \text{Yb}^{3+}, 2.5\% \text{Mg}^{2+}, 0.5\% \text{Nd}^{3+}$ NPs. The NPs were excited with a 980 nm femtosecond laser (observed as red spots). The HeLa cells were marked using the immunofluorescence method. Antibodies conjugated with Alexa Fluor 488 dye (excited by 488 nm argon laser) were attached to the lysosomes. The signal was collected in the range from 496 nm to 570 nm (observed as green regions). Nuclei stained with Hoechst 33 342 dyes were excited with a wavelength of 705 nm (blue colour). The signal was collected in the range from 423 nm to 475 nm. The images are a superposition of NPs luminescence, marked cells fluorescence, and nuclei fluorescence. (b) The spectra of NPs were excited by a femtosecond laser at a wavelength of 980 nm and an average laser power of 10%.

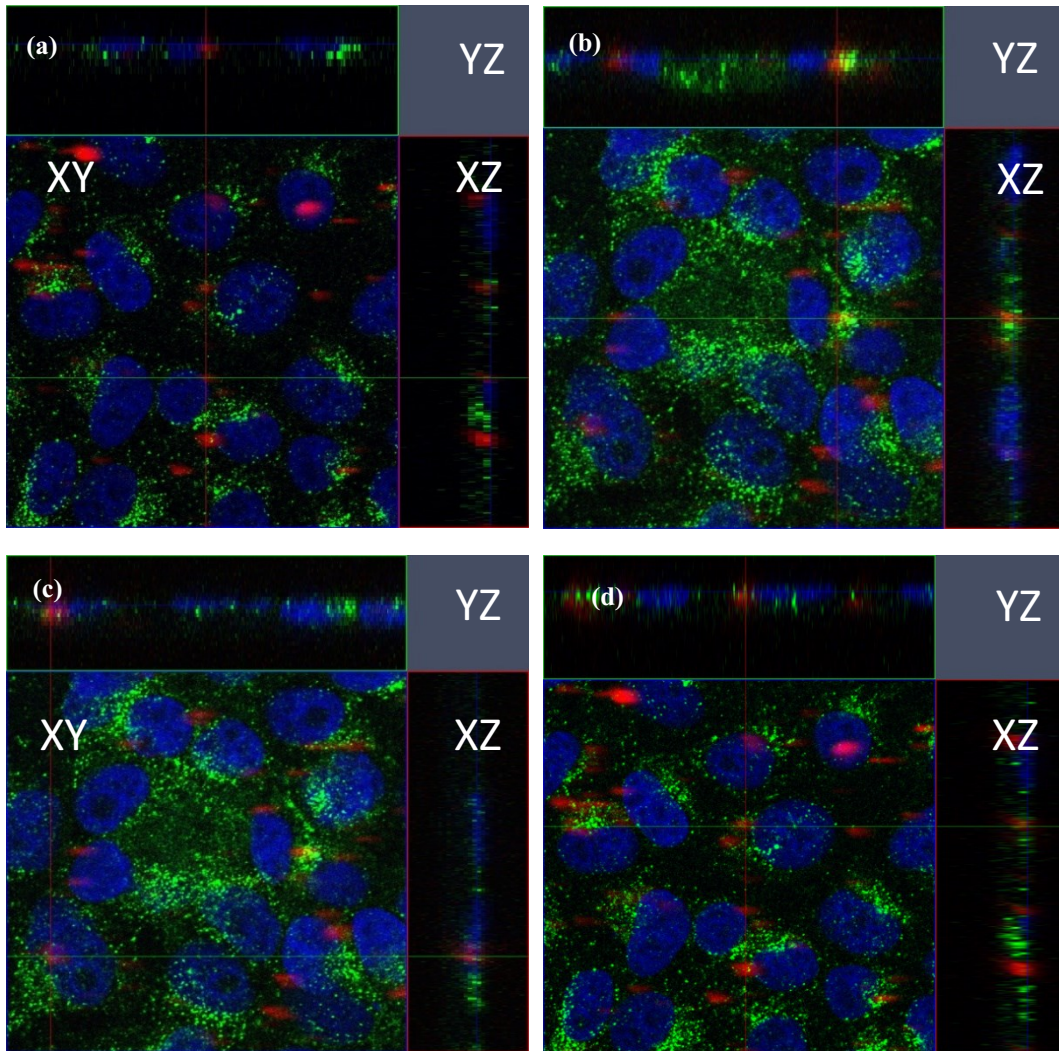


Fig. S31. (a)–(d) Confocal z-stack image of HeLa cells with $25 \mu\text{g}\cdot\text{ml}^{-1}$ of $\text{Fe}_3\text{O}_4/\text{Gd}_2\text{O}_3:1\% \text{Er}^{3+}$, $18\% \text{Yb}^{3+}$, $2.5\% \text{Mg}^{2+}$, $0.5\% \text{Nd}^{3+}$ NPs. The NPs were excited with a 980 nm femtosecond laser (observed as red spots). The HeLa cells were marked using the immunofluorescence method. Antibodies conjugated with Alexa Fluor 488 dye (excited by 488 nm argon laser) were attached to the lysosomes. The signal was collected in the range from 496 nm to 570 nm (observed as green regions). Nuclei stained with Hoechst 33 342 dyes were excited with a wavelength of 705 nm (blue colour). The signal was collected in the range from 423 nm to 475 nm. The images are a superposition of NPs luminescence, marked cells fluorescence, and nuclei fluorescence.